Materials Science & Engineering A 772 (2020) 138633

Contents lists available at ScienceDirect

Materials Science & Engineering A

journal homepage: http://www.elsevier.com/locate/msea

Steels in additive manufacturing: A review of their microstructure and properties

P. Bajaj [1], A. Hariharan [1], A. Kini [1], P. Kürnsteiner [1], D. Raabe, E.A. Jägle [*]

Department Microstructure Physics and Alloy Design, Max-Planck-Institut für Eisenforschung GmbH, Düsseldorf, Germany

ARTICLE INFO

Keywords:
Additive manufacturing
Steel
Review

ABSTRACT

Today, a large number of different steels are being processed by Additive Manufacturing (AM) methods. The different matrix microstructure components and phases (austenite, ferrite, martensite) and the various precipitation phases (intermetallic precipitates, carbides) lend a huge variability in microstructure and properties to this class of alloys. This is true for AM-produced steels just as it is for conventionally-produced steels. However, steels are subjected during AM processing to time-temperature profiles which are very different from the ones encountered in conventional process routes, and hence the resulting microstructures differ strongly as well. This includes a very fine and highly morphologically and crystallographically textured microstructure as a result of high solidification rates as well as non-equilibrium phases in the as-processed state. Such a microstructure, in turn, necessitates additional or adapted post-AM heat treatments and alloy design adjustments. In this review, we give an overview over the different kinds of steels in use in fusion-based AM processes and present their microstructures, their mechanical and corrosion properties, their heat treatments and their intended applications. This includes austenitic, duplex, martensitic and precipitation-hardening stainless steels, TRIP/TWIP steels, maraging and carbon-bearing tool steels and ODS steels. We identify areas with missing information in the literature and assess which properties of AM steels exceed those of conventionally-produced ones, or, conversely, which properties fall behind. We close our review with a short summary of iron-base alloys with functional properties and their application perspectives in Additive Manufacturing.

1. Introduction

The main advantages of additive manufacturing (AM) technologies of metallic parts compared to conventional synthesis and shaping processes lie in their ability to produce complex and/or customized parts with a short lead time, albeit in relatively low numbers. These advantages are exploited for example when patient-specific implants are produced, when complex, structurally optimized parts lead to performance-critical weight savings, or when AM is used for the repair of expensive metallic jet engine parts. The alloys usually envisaged in these applications are biocompatible, high temperature and lightweight materials such as Ti-, Ni-, Al- and Mg-based alloys. Consequently, reviews of alloys in AM have typically focussed on these materials [1–3], with two notable exceptions which do discuss steels, however with a different focus than the present review [4,5]. Yet, the most successful of all alloy families since the dawn of the iron-age 3000 years ago, namely steel, has received relatively little attention with respect to providing a holistic view of the interplay of alloy design, microstructure, properties and AM processing.

1.1. Scope of this review

In this review article, we aim to fill that gap by providing a review of the many different steels in use today in AM. Our focus is on the microstructures as well as the mechanical and electrochemical properties of steels made by fusion-based AM. In particular, we concentrate on the impact of the typical process conditions (thermal, chemical) operative during AM processing on the microstructure and properties. In contrast to the recent review by Fayazfar et al. [5], we do not describe in detail the AM process parameters required to achieve dense parts. We do discuss the impact of process parameters on the microstructure, where relevant. we restrict ourselves to fusion-based AM processes, in particular Laser and Electron-beam Powder-Bed Fusion (L-PBF and E-PBF) as well as Directed Energy Deposition (DED). Of these processes, the

* Corresponding author.
E-mail address: e.jaegle@mpie.de (E.A. Jägle).
[1] These authors contributed equally and are therefore listed in alphabetical order.

https://doi.org/10.1016/j.msea.2019.138633
Received 14 October 2019; Accepted 4 November 2019
Available online 7 November 2019

overwhelming majority of published studies are concerned with DED and L-PBF. While E-PBF is entirely capable of processing steels, its main applications today lie with other alloys.

We intentionally do not describe metal matrix composites (MMC) here. In particular in DED processing, which traces its roots to cladding (hardfacing) processes, there is a very high number of different steels reinforced by hard second-phase particles in use. Describing all of these in detail would lengthen this review excessively. We refer the reader to other reviews of this class of materials [3,6,7]. Additionally, we restrict ourselves to chemically homogeneous materials. This means that we do not give an exhaustive list of studies dealing with chemically graded specimens or AM of dissimilar alloys (multi-material approaches). Note that AM of graded specimens shares many similarities and challenges with dissimilar metals joining, which has been researched in the joining and welding community for many years.

1.2. Steel classes and their applications

Steels are the materials of choice in applications where the requirements are.

1. Corrosion resistance and general longevity under harsh environmental conditions
2. Strength, ductility, hardness, toughness and wear resistance
3. Low price
4. Unrivalled variety of achievable microstructure features ranging from ultra-hard martensite to compliant multiphase compounds, and/or
5. Functionalities such as ferromagnetism or invar effects.

The requirement of a good resistance to environmentally harsh conditions calls for stainless steels. Consequently, these steels, in particular AISI 316L/1.4404, are used in a large variety of applications where the parts to be fabricated are expected to come into contact with corrosive media at moderate temperatures during service. Where an overlap of corrosion resistance and increased mechanical strength and hardness (compared to austenitic stainless steels) is required, maraging-type precipitation-hardened martensitic stainless steel grades are often used (so called PH steel grades such as 17-4PH/1.4542 and 15-5PH/1.4545). This is e.g. the case in marine, power-plant and injection moulding industries [8].

Good yield strength, high hardness and abrasion resistance are required in the tool and die making industry, calling for tool steels. The key advantage of AM in this application is the ability to manufacture many separate, smoothly curved cooling channels close to the surface contour of e.g. injection moulding tools, leading to an efficient heat removal and thus an increased productivity and/or lifetime of the tool [9–14]. The tool steels most used in conventional toolmaking processes contain a significant amount of carbon and are not easy to process, as will be described later, and thus the most popular choice of tool steel in AM processing today are the carbon-free maraging steels, in particular 18Ni-300/1.2709 [5].

The comparably moderate price of stainless steels and their good processability also leads to austenitic stainless steels often being considered a good material for users new to AM.

Besides these main groups of steels, there is a number of other, less studied alloys in use in AM. They include for example martensitic stainless steels, duplex stainless steels, TRIP/TWIP steels and oxide-dispersion strengthened (ODS) steels. Functional application fields for steels such as custom shaped parts for electro-magnetic or invar applications require the use of Fe–Si, Fe–Ni or Fe–Co alloys.

1.3. Organization of this article

To allow the reader to gain a structured overview over this wide field, we group in the following the steel grades according to their main microstructural constituents at room temperature. We begin by describing fully austenitic (stainless) steels, progress to TRIP/TWIP steels, which are in the undeformed state austenitic and then move to duplex steels, which consist of a combined austenitic/martensitic microstructure. Next, we describe martensitic and precipitation hardening stainless steels. These are fully martensitic if processed by conventional process routes. Similarly, maraging and carbon-bearing tool steels are normally employed in an aged/tempered martensitic state. Finally, we describe ODS steels, which are usually particle-reinforced fully ferritic stainless steels. This grouping relates to the microstructural constituents as they are present after conventional processing. As will become clear from the individual sections below, processing by AM does not always lead to the intended phase composition so that not all of these materials fall readily into one of these microstructure categories when subjected to AM processing.

Within each section, we describe the microstructure of the material, the phases present in the as-produced and heat-treated state and its crystallographic texture. We summarize the static mechanical properties and, where enough data is available in the literature, the fatigue properties. Where appropriate, we also describe additional properties of the steel such as the magnetic and corrosion properties. We close our review with an outlook on new developments in the field of steels for AM, which includes steels with functional properties.

1.4. Overview over composition and tensile properties of the steel classes

In Table 1, the chemical composition of the most widely used steel grades in each of the described alloy classes are given, together with the usually used grade name. In Fig. 1 and Fig. 2, schematic overviews over their basic mechanical properties as well their microstructure after AM processing are presented. For comparison, also the values and microstructure for equivalent, conventionally-produced steels are given. The figures serve are intended to provide a broad overview over the results reported in the literature, but do not in all cases capture the sometimes considerable dependence of the microstructure on processing parameters.

2. Austenitic microstructure: stainless steels and TRIP/TWIP steels

2.1. Austenitic stainless steels (ASS) in use in AM

The published literature in AM of austenitic stainless steels is almost exclusively restricted to 316L stainless steel (1.4404, X2CrNiMo17-12-2), with some reports in the literature about 304L stainless steel (1.4307, X2CrNi18-9). In these steels, the high chromium content (17-18 wt.-%) leads to a good corrosion resistance, while the nickel additions keep the microstructure of the alloys fully austenitic in conventionally-produced materials. To the best of our knowledge, there are no reports on the 200-series of austenitic stainless steel, where Ni is replaced by Mn as austenite stabilising element.

2.2. Early attempts to process austenitic stainless steels by AM

Today, austenitic stainless steels are processed routinely in L-PBF, yielding fully dense material. The stainless steel 316L was already used in some of the very earliest papers demonstrating laser powder-bed fusion, i.e. full melting of the powder instead of partial sintering or melting of a second-phase binder material with a low melting point. However, these attempts in the early 2000s were only partially successful because of the strong balling effect during the process, where molten metal forms spheres owing to a high surface tension and thus poor wetting of the substrate [15]. Balling can be attributed to a low laser power, a large focus diameter and hence a low laser energy per unit area. Typical values at that time were a maximum power of 50 W and a beam diameter of 0.8 mm. Contributing factors to balling were the poor

Table 1
Chemical composition of the most widely used grade of each steel class. All compositions in wt.-%, Fe content is balance. If no value is given, the content is unspecified or as low as possible.

Type	Commonly used grade name	C	Cr	Ni	Mo	Mn	Si	Ti	Al	Other
austenitic stainless steel	**316L** (AISI standard)	<0.03	16–18	10–14	2.0–2.5	<2	<0.75			
Duplex stainless steel	**SAF2705** (brand name)	<0.03	25	7	4	<1.2	<0.8			
PH stainless steel	**17–4 PH** (brand name)	<0.07	15–17	3–5		1	1			3-5 Cu
Maraging tool steel	**18Ni-300** (MIL standard)	<0.03	<0.5	17–19	4.5–5.2	<0.1	<0.1	0.6–0.8	0.05–0.15	8.5–9.5 Co
C-bearing tool steel	**H13** (AISI standard)	0.32–0.45	4.75–5.5		1.1–1.75	0.2–0.6	0.8–1.2			0.8–1.2 V
ODS steel	**PM2000** (brand name)	0.07	19	0.03	0.13	0.07		0.5	4.2	0.5 Y_2O_3

oxygen control in the process chamber and the coarse powder (mean diameter of 75 µm) in use [15]. Continued attempts during the next decade with varying powder size and process parameters coupled with thermal modelling and single track experiments (cf. Fig. 3) resulted in identification of a process window to avoid balling and produce solid components in the L-PBF process [16–18]. Still, the lasers in use had a limited power and large beam diameters compared to today's standards, with typical values up to 200 W and between 0.5 and 1.1 mm, respectively. This resulted in rather slow possible build rates with scan velocities ranging from 0.5 to 50 mm/s [16]. Finally, in 2010 Tolosa et al. achieved a relative density greater that 99.9% in L-PBF produced 316L stainless steel using a 200 W laser with a 80 µm laser focus diameter and scan velocity of up to 1000 mm/s [19,20]. Efforts in process development are now directed towards developments of machine independent standard process parameters. Kamath et al. suggest the use of the energy density (roughly: the energy imparted by the laser beam divided by the volume of the melt pool) to identify process parameters required to produce components with more than 99% relative density [21]. Thomas et al. suggest the use of process maps based on normalized energy density [22]. Bajaj et al. define a criteria of dimensionless overlap depth,

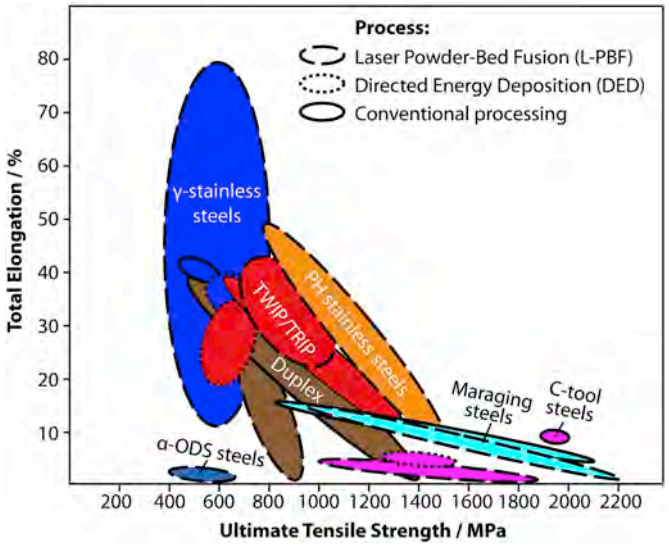

Fig. 1. Overview over basic mechanical properties of steels discussed in this reviews, to allow a general comparison of properties obtained by conventional processing and by the 2 a.m. processes DED and L-PBF. The kind of steel is denoted by field colour, while the field border indicates the method of production. Generally, the properties in heat treated state, where applicable, are given. All data sources are mentioned in the individual chapters of this review. ODS: Oxide Dispersion-Strengthened, C-tool steels: Carbon-bearing tool steels, TWIP/TRIP: Twinning/Transformation-induced Plasticity, PH: precipitation hardening. (For interpretation of the references to colour in this figure legend, the reader is referred to the Web version of this article.)

calculated from process parameters using analytical models, being greater than 1 for producing parts with relative density greater than 99% [215]. Other recent works are focussed on increasing production rates of L-PBF process. For instance, Metelkova et al. used a larger laser beam diameter together with higher laser power to increase the productivity by up to 840% [23].

2.3. Microstructure of as-built austenitic stainless steels: phase selection and hierarchical nature

The microstructure in L-PBF produced stainless steels has been reported to be fully austenitic and to have a columnar grain structure with fine solidification cells with diameters of 1 µm or less [1,24–27]. Note that these solidification cells are very similar in crystallographic orientation, so many tens or hundreds of such cells together form one austenite grain, i.e. a material volume bound by high angle grain boundaries (see Fig. 4b and c). The grains observed in L-PBF produced stainless steel samples are finer than the ones in conventional processes [24,26–29]. 316L and 304L stainless steels are in a composition range where solidification can occur either with a primary (δ-) ferritic phase or with a primary austenitic (γ) phase. The different primary solidification phases and their impact on the final microstructure and properties of these alloys are well documented e.g. in the welding literature [30,31]. In DED processing of 316L stainless steel, it is indeed observed that in the regions along the borders of the solidification cells (i.e. in the intercellular regions), the microsegregation during solidification leads to an enrichment in the ferrite stabilising elements Cr and Mo and hence to fine ferritic films (up to 9 vol.-%) [32,33]. The primary solidification phase in this case is austenite, as expected from the Schaeffler diagram [33]. In L-PBF, however, the observed microstructure in all studies is fully austenitic and there is no indication of any solid-state phase transformation [24,29,34–36]. This observation is in line with results obtained in rapid solidification experiments (splat quenching and laser welding), where it was shown that a higher cooling rate favours partitionless austenitic solidification [37]. In the case of L-PBF, the solidification is however not entirely partitionless. The intercellular regions show an enrichment with Cr and Mo, which is, however, not sufficient to stabilise ferrite [27,38].

Despite this seemingly simple microstructure, austenitic stainless steels produced by L-PBF display an outstanding combination of higher strength than their conventionally produced counterparts without a reduced ductility. Wang et al. attribute this property combination to the hierarchical nature of the microstructure (cf. Fig. 4), consisting of solidification cells, low and high angle grain boundaries, dislocations, and oxide inclusions [38]. This hierarchy spans six orders of magnitude on the length scale and is unique to AM processing. Similar hierarchical microstructures have also been reported in Electron Beam Powder Bed Fusion (E-PBF) of stainless steel 316L [39].

Wang et al. also show that the microstructural features can be controlled via process parameters and propose tuning of the

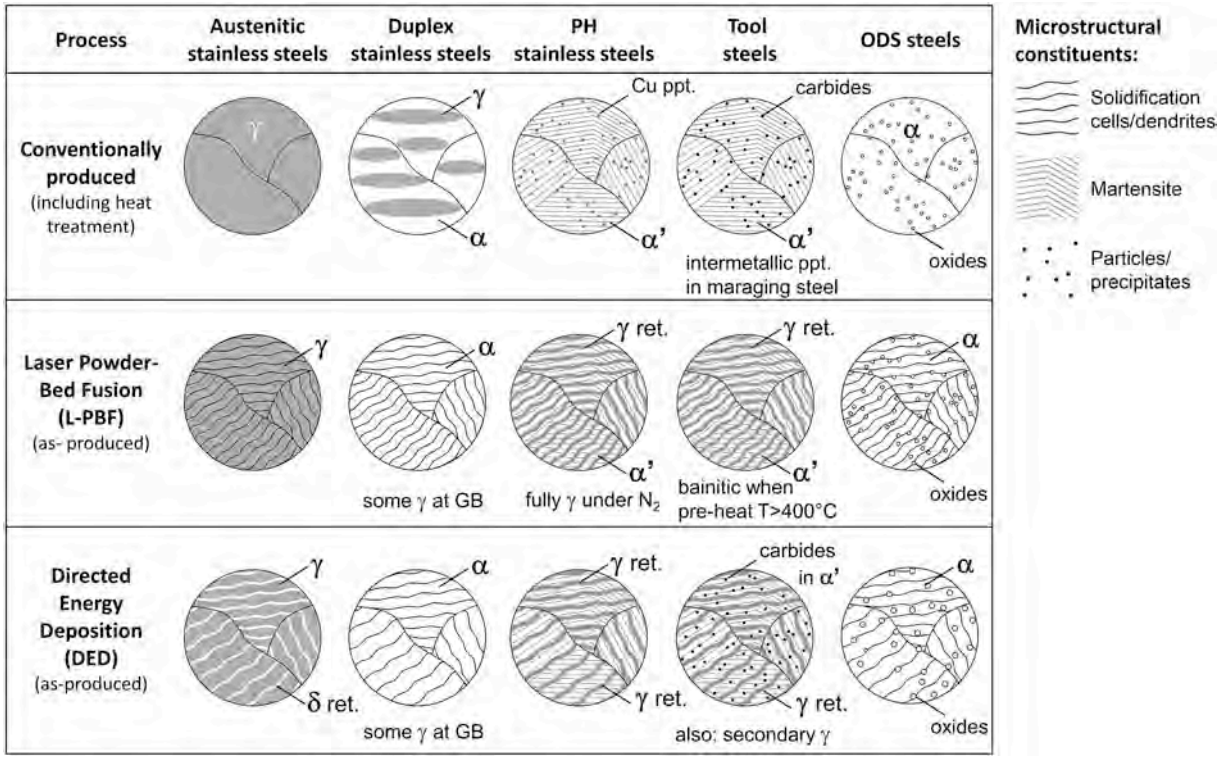

Fig. 2. Overview over typical microstructures of the different steels in this review, produced conventionally (in the state intended for use) and after additive manufacturing. Only the 2 a.m. processes L-PBF and DED are depicted due to limited information available for E-PBF in the literature. Note that depending on processing conditions, different microstructures may be observed after AM. ppt.: precipitates, ret.: retained, α: ferrite, bcc, α': martensite bcc/bct, γ: austenite, fcc.

microstructure on a layer-by-layer basis or even within individual layers [38]. The possibility to control cooling rates during and after solidification by varying process parameters presents an opportunity to exert local and digital control over the steel microstructure, impossible in conventional methods. Todd suggests using these to precisely control microstructures at a fine scale to unlock the potential of existing alloys in terms of mechanical properties [40].

Upon plastic deformation, austenitic stainless steels typically show strain-induced martensite formation. The high yield strength, combined with a low work hardening rate observed in L-PBF produced 316L is due to the fact that the martensite formation is hindered in the very fine microstructure [41]. This obstruction is particularly pronounced at cryogenic temperatures. Agnew et al. argue that the high elongation to fracture observed in L-PBF produced 316L is the result of work hardening from twinning induced plasticity (TWIP) [42].

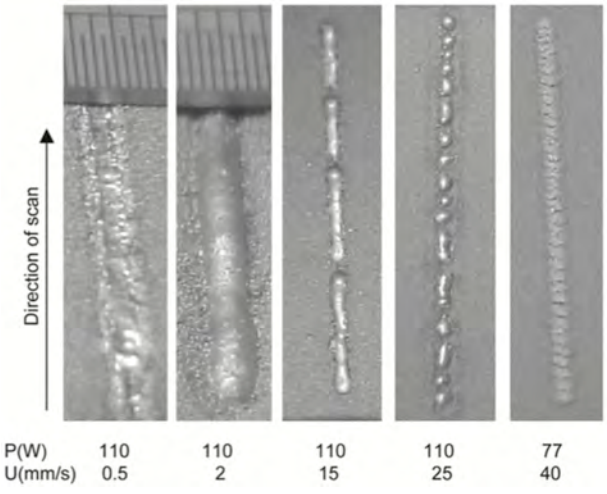

Fig. 3. Early single-track experiments to identify suitable process parameters for L-PBF processing of 316L austenitic stainless steel. Reprinted with permission from Ref. [16].

2.4. Texture and texture control of austenitic stainless steels

Usually, a strong crystallographic fibre texture with the <001> direction aligned along the build direction (i.e. against the direction of fastest heat removal) is observed [29,36]. However, depending on scanning strategy such a strong crystallographic texture is sometimes not present [24,26]. The texture is usually explained by the fact that the <001> direction is the fastest growing direction in the solidification of cubic metals, and hence dendrites/cells grow with this crystallographic orientation aligned with the temperature gradient [4]. The temperature gradient, in turn, is dictated by the heat removal from the melt pool, which is globally dominated by conduction towards the base plate (i.e. along the build direction), but locally varies along the melt pool. As explained below, by modifying the process parameters such that the melt pool shape and the fraction of each melt pool that gets re-melted with each scan track and each layer is altered, the overall texture of the material can be influenced.

Sun et al. demonstrate an approach to achieving high strength and ductility in L-PBF produced 316L by enhancing the TWIP effect [44]. They modify the crystallographic texture along the build direction from the usual <001> to <110> using a scanning strategy including small hatch spacings and a relatively high laser power. The <110> grain orientation favours twinning upon deformation and leads to higher strain hardening rates which in turn simultaneously improves UTS and ductility. Sun et al. later demonstrated that by careful control of the laser parameters in L-PBF it is even possible to attain a crystallographic lamellar microstructure (see Fig. 5 c) in 316L, where, <100> and <110> oriented grains along the build direction are present alternately [43]. Texture control can also be used to avoid the anisotropy in yield

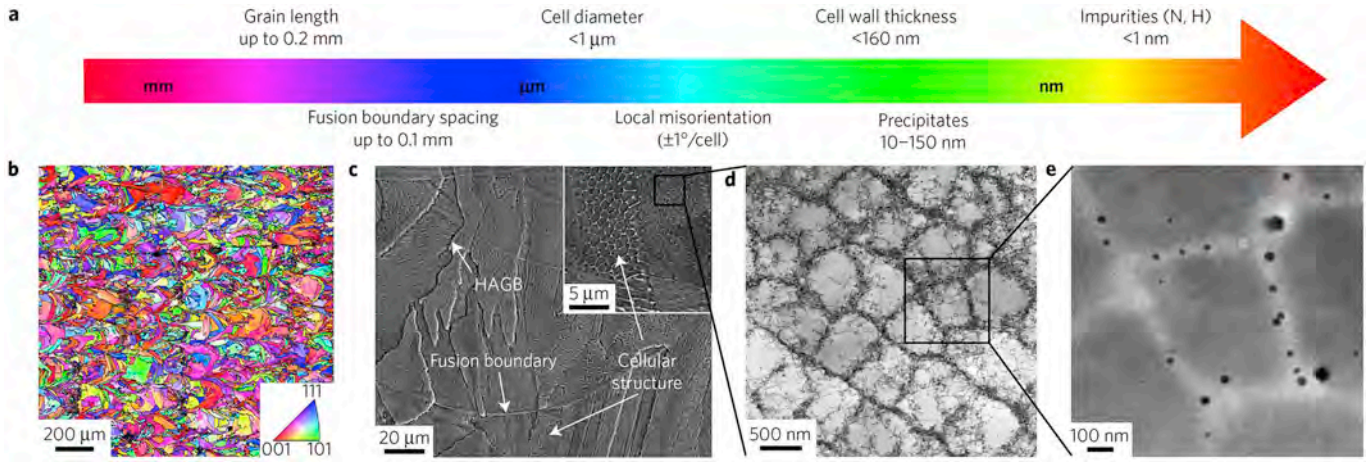

Fig. 4. Microstructural features of an L-PBF produced 316L austenitic stainless steel at different length scales. a) Schematic showing the various length scales of the microstructural features observed. b) EBSD inverse pole figure mapping showing the grain orientations. C) SEM image of the cross section showing high-angle grain boundaries (HAGB), fusion boundaries (delineating melt pools), and the cellular solidification structure. d) Bright field TEM image of the cellular structure showing dislocation networks in the cell boundaries. e) high-angle annular dark-field (HAADF) scanning TEM (STEM) image of the solidification cells showing oxide particles. Figure reprinted with permission from Ref. [38].

and tensile strength [42]. However, the strain hardening behaviour is highly dependent on the grain morphology, resulting in anisotropy in ductility despite reduced texture [42].

2.5. Heat treatments of as-built austenitic stainless steel parts

Riemer et al. perform stress relieving heat treatments up to 650 °C and report a stable microstructure [29]. This is supported by Saeidi et al. who do not find microstructural changes up to annealing temperatures of 800 °C (cf. Fig. 6) [45]. Higher annealing temperatures, both in a furnace and in a HIP, lead to recrystallization of the material. Saeidi et al. observe a partial transformation to δ-ferrite needles at annealing temperatures of 1150 °C or higher, as predicted by the equilibrium phase diagram. This ferrite is stable upon slow cooling to room temperature and, together with the recrystallization and coarsening phenomena, leads to a loss of strength of the material [45].

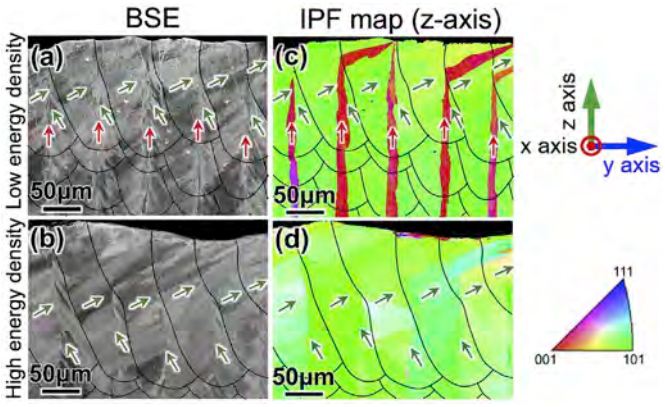

Fig. 5. a), b) Backscattered electron (BSE) SEM images showing melt pool boundaries and columnar grain structure along the y-z (scanning direction – build direction) plane for a sample prepared using low energy density (a) and high energy density (b). C), d) EBSD inverse pole figure maps along z axis (build direction) corresponding to (a) and (b). The process parameters impact the texture by re-melting different parts of the material. Figure adapted from Ref. [43] and reused under Creative Commons Attribution License (CC BY).

2.6. Tensile properties of austenitic stainless steel compared to conventionally produced material

As qualitatively described before, L-PBF produced stainless steels often have superior yield strength and tensile strength [26,27,29,38,42,46–48]. The reported values show a high variability and are in the range of 350–600 MPa and 480–800 MPa for yield strength and UTS, respectively. Conventionally produced steel shows typical values of 230–290 MPa and 580–590 MPa for YS and UTS [49] (see Fig. 7 for a comparison). L-PBF produced material also has a higher yield to tensile strength ratio [26,29,46,48]. Although some works report lower fracture toughness and elongation to failure (as low as 12%) for L-PBF produced stainless steel as compared to wrought material [26,50] (typically: 40–50%), most studies report a higher elongation to failure and fracture toughness (up to 67%) [27,29,38,42,48,51]. The high tensile and yield strength have been related to the finer microstructure and dislocation substructure as per Hall-Petch relation [27,38,42,47]. As with all AM-produced alloys, the defects in the material (brittle phases/inclusions, porosity) have a strong impact on the elongation to fracture. For a tabular overview of the tensile test properties determined by many different authors for stainless steels produced by L-PBF, E-PBF and DED, we refer the reader to the tables in the reviews by Herzog et al. [1], Lewandowski and Seifi [49], and Fayazfar et al. [5]. Generally, the values reported for DED and E-PBF fall within the large range of values reported for L-PBF-produced austenitic stainless steel, as can be seen in

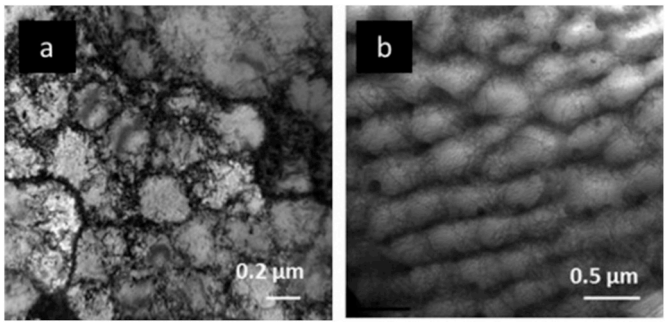

Fig. 6. TEM images for a) as L-PBF produced and b) heat treated (800 °C for 1 h) 316L stainless steel. Annealing at this temperature results in reduction in dislocation density but the cellular structure and the cell size remains unchanged. Reprinted with permission from Ref. [45].

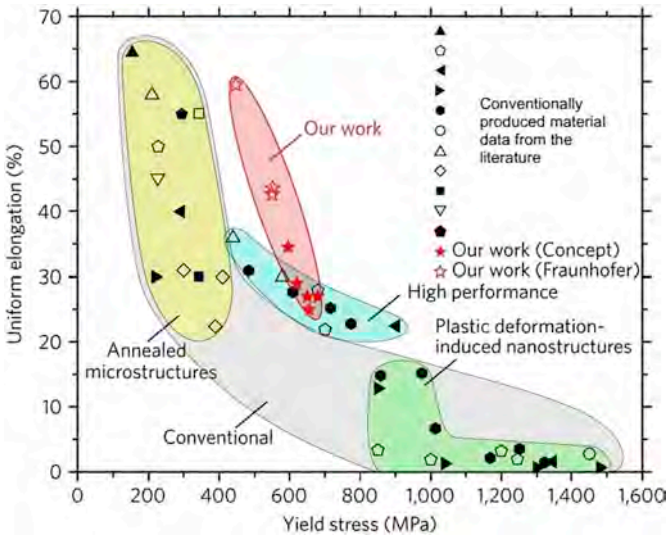

Fig. 7. Tensile mechanical properties of L-PBF produced 316L austenitic stainless steel compared with the properties of conventionally-produced material. The improved yield strength at similar uniform elongation values of L-PBF material compared to annealed conventionally produced material can be clearly seen. Figure adapted with permission from Ref. [38]. The references for the conventionally-produced material properties taken from the literature are available in the original publication.

the overview Fig. 1.

In DED produced stainless steels, a lower yield and tensile strength is observed at the top of the sample than near the base plate. This is the result of lower cooling rates further away from the substrate, where heat conductivity away from the laser heat source is slower [32,52] (we will return to this point in greater detail in the section dealing with tool steels).

2.7. Fatigue properties of austenitic stainless steel

Fatigue strength of L-PBF produced stainless steel samples is an important factor for applications in areas such as the medical or aerospace industry [26,29,53]. As can be expected, there is a difference to conventionally produced materials. Firstly, the elongated grain structure (composed of many solidification cells, elongated in the same direction as the grains) in L-PBF produced samples results in a different crack growth behaviour depending on the loading direction (see Fig. 8). For loading parallel to the direction of grain growth (Fig. 8 b), the crack path is highly tortuous, resulting in slow growth. On loading perpendicular to the grain long axis, the crack propagation along grain boundaries is straight and unhindered (Fig. 8 a) [26,29]. Stress relieving

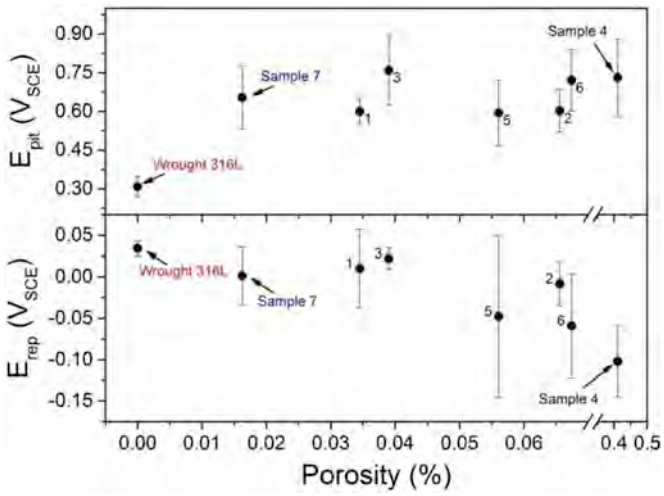

Fig. 9. Pitting and repassivation potentials of L-PBF produced 316L austenitic stainless steel compared to conventionally-produced material. While the resistance to pitting is higher, the repassivation of pits also requires a higher potential. Figure reprinted under Creative Commons license (CC-BY-NC-ND 4.0) from Ref. [55].

heat treatments up to 650 °C do not alter the grain structure and therefore do not have any significant effect on the crack propagation [29]. Hot isostatic pressing (HIP) processing at even higher temperatures, on the other hand, results in partial recrystallization and therefore in a bimodal, more isotropic microstructure yielding isotropic crack propagation [29]. High surface roughness of the as L-PBF built samples is particularly detrimental to their fatigue performance and it was observed that the fatigue limit can be improved by as much as a factor of two when introducing a surface finishing step [29,53]. Stress relief heat treatments and HIP both have only a small effect on the fatigue performance, but largely, after surface finishing, the fatigue limit is in the range of conventionally processed samples [26,29,53].

2.8. Corrosion properties of austenitic stainless steel

Recent studies have shown that L-PBF stainless steels have better corrosion resistance properties as compared to wrought material [43,54,55]. Sander et al. show that L-PBF produced stainless steel 316L is more resistant to pit initiation as compared to wrought 316L, however, L-PBF samples also had inferior repassivation once a stable pit was initiated (cf. Fig. 9) [55]. The Cr-depleted zone around MnS inclusions is known to be a pit nucleation site, and thus the better resistance to pit initiation in L-PBF material can be attributed to small or non-existent MnS inclusions [50,55]. The size of MnS is smaller in L-PBF-produced material compared to conventionally-produced material presumably due to the

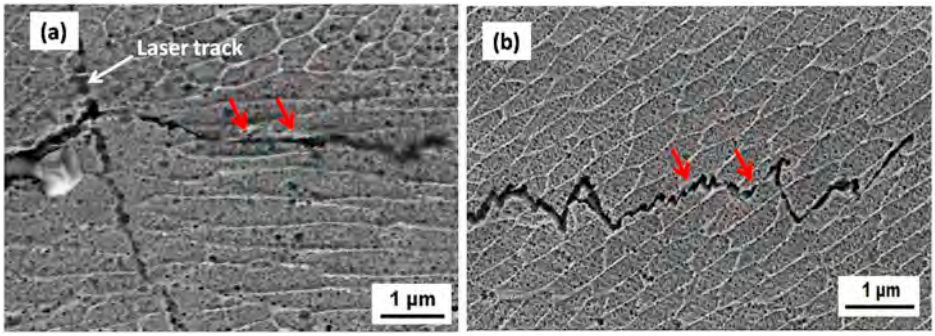

Fig. 8. Cross sectional SEM image (backscattered electron contrast) showing fatigue crack growth interaction with solidification cell structure in loading perpendicular to the grain long axis (a) and parallel to it (b). Note that grains are elongated and coaxial with the solidification cells. Since the crack progresses preferentially along the cell boundaries, the crack tortuosity depends on loading direction. Reproduced with permission from Ref. [26].

high cooling rate during solidification [56,57]. This is observed also with other primary precipitates in L-PBF-produced materials [58]. The small oxides/oxynitrides present in the material apparently do not act as pit initiation sites [57]. The lamellar microstructure obtained by Sun et al. leads to an extremely high corrosion resistance with breakdown (pitting) potential approaching the stability limit of chromium oxide [43]. Lau et al. studied the potential of L-PBF stainless steels to be used in nuclear applications [50,59,60]. In consecutive papers they show that after high temperature recrystallization, the fatigue, impact, and stress corrosion cracking behaviour of L-PBF 316L is comparable to wrought alternatives and is suitable for use in nuclear applications under elevated temperatures.

2.9. Other austenitic stainless steels

In general, AM produced 304L stainless steel is very similarly to the previously described 316L stainless steel in terms of microstructure and properties. The rationale for its use lies in its lower Ni content which leads to a reduced price, but also a reduced austenite stability. Abd-Elghany et al. demonstrated L-PBF of 304L stainless steel, however, due to poor density they only achieved yield and tensile strengths of about 70% as compared to wrought products [35]. Nonetheless, they were able to obtain a fully austenitic microstructure devoid of any grain boundary carbides. Later, Guan et al. manufactured almost fully dense samples resulting in yield and tensile strengths of up to 570 and 717 MPa respectively, both higher than the wrought alternatives [48]. They also reported a higher yield to tensile strength ratio of ~0.8. They also showed the effect of scan strategy on the isotropy of the microstructure and related it to the mechanical properties. Wang et al. performed DED of 304L [52]. They studied the effect of chemical composition on the austenite stability and mechanical properties as a result of strain hardening. They observed that lower content of austenite stabilizers, either achieved intentionally by mixing of pure Fe powder with pre-alloyed 304L or by evaporation of austenite stabilizers during the process, reduces the austenite stability which promotes strain hardening by TRIP effect and results in a superior UTS and elongation to failure.

2.10. TRIP/TWIP steels

TRIP and TWIP steels are usually fully austenitic metastable steels that show deformation-induced transformation (TRIP) or twinning (TWIP) upon plastic deformation. In this property, they are not unlike the aforementioned austenitic stainless steels. The high work hardening capacity of these steels make them attractive for applications where high energy absorption, high strain hardening rates and high ductility are required.

There are a few studies reporting on the development and use of TRIP/TWIP steels in AM. Haase et al. processed a high-manganese steel (X30Mn22) by L-PBF and investigated its microstructure and deformation behaviour [61]. In the as-produced state, the microstructure consisted mainly of austenite, together with α′- and ε-martensite. Mn segregation was present, but much reduced as compared to cast reference material. They showed that the TRIP/TWIP effect is indeed operational upon tensile deformation of the material and discuss its anisotropy stemming from the strong, L-PBF-typical fibre texture. For all testing directions, the yield strength and UTS were found to be higher compared to cast and rolled reference material (302–416 MPa vs. 275 MPa and 906–1065 MPa vs. 894 MPa, respectively), but the elongation at fracture is less (24–31% vs. 52%). The same group also shows production of the same steel, but with varied Al additions by DED and L-PBF [62]. By increasing the Al content, the stacking fault energy of the material increases, which leads to a change in deformation mechanism from TRIP to TWIP, as well as a suppression of martensite formation in the as-produced microstructure. Another study employs the commercial TWIP steel X–IP 1000 (X60Mn22), processed by L-PBF [63]. The material displays mechanical properties similar to its conventionally processed counterpart and a strong crystallographic texture. The authors also report on L-PBF processing of the same steel modified by Ag additions for improved electrochemical dissolution rates intended for use in biodegradable implants [64].

3. Austenitic/martensitic microstructure: duplex stainless steels

Duplex stainless steels are used due to their very good corrosion resistance, in particular against pitting and crevice corrosion [65]. As the name suggests, their microstructure consists of a combination of ferrite and austenite, typically in roughly equal amounts. Despite similar concentrations of the austenite-stabilising Ni as in austenitic stainless steels (and additionally some N in the “superduplex” grades), ferrite is stabilized by the very high content of Cr (24–26%). This is primary δ-ferrite that forms upon solidification, while austenite forms during cooling or during heat treatments. As can be expected, changes in processing can have a strong impact on the phase composition. Most of the few published works on AM of duplex stainless steels pertain to the "superduplex" steel 2507 (1.4410, X2CrNiMoN25-7-4).

3.1. Phase selection, microstructure and texture of duplex stainless steels in as-produced and heat treated state

In the first study on L-PBF processing of duplex steel, relative densities of only 90% were achieved [66]. Nevertheless, already in this study it was established that L-PBF processing leads to an almost exclusively ferritic microstructure with small amounts of austenite and nitrides (presumably Cr_2N) nucleating at grain boundaries. The higher the laser energy input is, the more time austenite has to grow at elevated temperatures, and hence the higher the final austenite fraction in the microstructure is. Note that the growth morphology of austenite is along grain boundaries or of Widmanstätten type. A post-heat treatment allows to reach the desired phase mixture of 55% austenite and 45% ferrite. Subsequent studies reached >99.5% relative density and confirmed the microstructural findings, including the absence of σ phase in the as-produced state [67]. The σ phase is an intermetallic phase in Cr-rich steels that is generally detrimental to the ductility and is therefore unwanted. Due to the exclusively ferritic microstructure in the as-produced state, the yield strength and UTS of L-PBF produced 2507 is much higher compared to conventionally produced material, with a moderate elongation at fracture of 8% and a ductile fracture mode. Heat treatment at 1200 °C leads to the desired α+γ microstructure, but also to the formation of σ phase precipitates [68]. This renders the steel quite brittle at room temperature (1.8% elongation at fracture) and softer (920 MPa UTS), due to the presence of austenite. Hengsbach et al. study the heat treatment response of L-PBF-produced UNS S31803 duplex stainless steel and find that recrystallization is taking place at all studied temperatures from 900 to 1200 °C and that the maximum austenite fraction is obtained at the intermediate temperature of 1000 °C [69] (see Fig. 10 for a comparison of as-built and recrystallized micro- and nanostructure). They also remark that some nitrogen is lost during the L-PBF process, without quantifying it.

Eriksson et al. demonstrate the processing of Zeron 100X, a superduplex stainless steel, by wire and arc additive manufacturing (WAAM) [70]. Due to the significantly slower cooling rate in this AM process, compared with L-PBF, there is a high fraction of austenite and chromium nitrides already present in the microstructure after cooling. Additionally, the intrinsic heat treatment of subsequent passes (IHT, cf. Section 5 on tool steels) leads to the precipitation of secondary austenite.

3.2. Magnetic properties of duplex stainless steels

Another consequence of the high ferrite fraction of AM-produced material is that the magnetic properties differ markedly from conventionally-produced material: The saturation magnetization and the coercivity in L-PBF processed 2507 duplex steel are both much

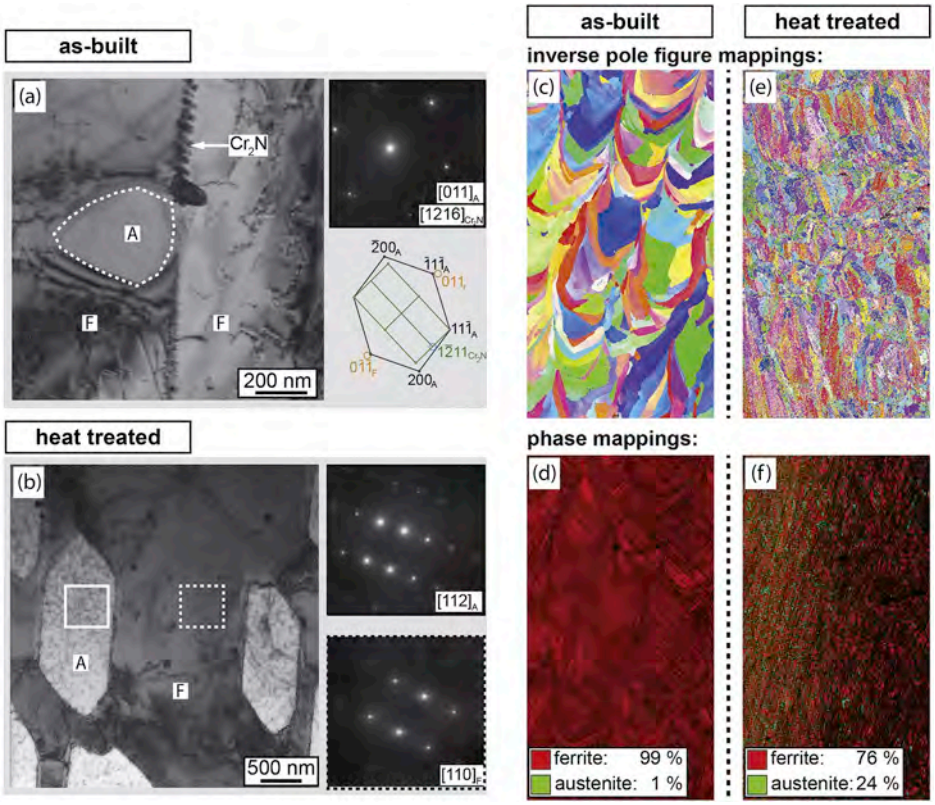

Fig. 10. TEM images of L-PBF produced UNS S31803 duplex stainless steel in the (a) as-produced state and (b) in the heat treated state. (c–f) EBSD (electron backscatter diffraction) inverse pole figure and phase mappings of the same material. Contrary to conventionally-produced duplex stainless steel, the L-PBF material is almost fully ferritic in the as-produced state, with small austenite grains and chromium nitride precipitates along the grain boundaries. A suitable heat treatment partially recovers the desired duplex austenite/martensite microstructure. Adapted with permission from Ref. [69].

higher than in its conventionally-produced counterpart [71]. Additionally, the AM-typical strong fibre texture also leads to a pronounced anisotropy in the soft magnetic properties.

4. Mainly martensitic microstructure: martensitic and precipitation-hardening stainless steels

Precipitation-hardened (PH) stainless steels combine a high corrosion resistance and mechanical strength. They are promising for AM production due to their good weldability. There are fully martensitic and austenitic/martensitic grades [72]. The two PH steels practically exclusively in use in AM today are 17-4 PH (1.4542, X5CrNiCuNb16-4) and 15-5 PH (1.4545, X5CrNiCo15-5), both usually called "fully martensitic" grades. PH steels contain Cr (in the range of 16–18 wt%), Ni and Cu (3–5 wt % each). The chromium content is responsible for the corrosion resistance of PH steels by forming a passive layer of Cr_2O_3 oxide [73]. Nickel is an austenite stabilizer, which also enhances the corrosion resistance. Precipitation hardening is due to the Cu precipitates in the microstructure, which nucleate and grow upon ageing heat treatment. In comparison to the 17-4 PH grade, 15-5 PH steel has a slightly lower chromium content and minor additions of molybdenum. There are other PH steel grades which do not rely on Cu as precipitation strengthening element, such as 17-7 PH (1.4568, X7CrNiAl17-7), or commercial alloys such as stainless steel EOS CX [74] or Uddeholm Corrax. These achieve precipitation hardening instead by an addition of Al, forming the Ni_3Al phase, which renders them closely related to maraging steels (see the next section). There are very few studies on AM of martensitic stainless steels (i.e. non-precipitation-hardening). These steel grades (400 series stainless steels) contain Cr at similar levels as in austenitic stainless steels (usually 12-14 wt.-%) but no or a low amount of C and Ni which is insufficient to stabilise austenite at room temperature.

Due to the high number of studies on 17–4 PH steel, mostly using the L-PBF process, we first describe the microstructure and properties of this material-process-combination and how they compare with their wrought (conventionally produced) counterpart. Next, we describe other AM processes and the properties of 15–5 PH and other martensitic stainless steel grades.

4.1. Microstructure and texture of PH stainless steels

Wrought 17–4 PH steels usually have a fully martensitic (BCC) microstructure [8]. However, the presence of austenite-stabilising Ni makes it relatively common to also find retained austenite in the microstructure. The martensite finish temperature is only slightly above room temperature (32 °C), so small variations in steel chemistry and processing can have a pronounced effect on the phase composition.

Extensive studies on the effect of AM process parameters and post heat treatment on the relative density, final microstructure and mechanical properties of 17-4 PH have been performed [75–81]. The as-produced microstructure can contain a high fraction of austenite phase or can even be fully austenitic, despite the high cooling rates during L-PBF. For example, Facchini et al. report that L-PBF-produced 17–4 PH stainless steel (Ar process atmosphere) contains 72% austenite and 28% martensite [82]. TEM investigations show retained austenite sandwiched between martensite plates. The as-produced microstructure can additionally contain Nb-rich carbides (cf. the SEM micrograph and the EDS maps in Fig. 11) [83].

Both ferritic/martensitic and austenitic as-produced 17–4 PH usually exhibits the AM-typical strong crystallographic fibre texture with the <001> direction along the build direction [84,85]. In Fig. 12, the microstructure of L-PBF produced 17–4 PH steel is displayed as EBSD inverse pole figure and phase maps. The (in this case only moderate) volume fraction of retained austenite is clearly visible. It must be noted that many studies only note the fraction of austenite and martensite/-ferrite without unravelling the complex spatial distribution of phases and its origin by solidification and solid-state phase transformations. Generally, there is a much larger variability in the reported

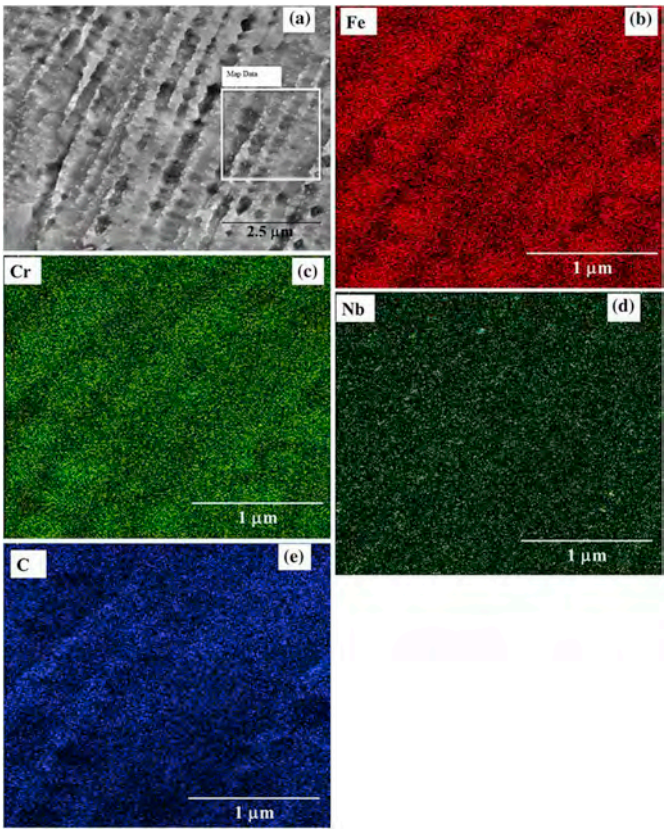

Fig. 11. SEM image showing the presence of fine NbC precipitates in interdendritic regions in as-built 17–4 PH stainless steel. (b–e) EDS maps acquired from the highlighted region in (a) giving evidence for the enrichment of Fe and Cr in dendrite cores and Nb and C in interdendritic regions. Reprinted with permission from Ref. [83].

microstructures as compared to other steel types.

4.2. Reasons for the high variability in the observed microstructure if PH stainless steels

Several explanations for the strong discrepancy between microstructure in as-quenched conventional material (fully martensitic) and as-L-PBF-produced material (up to fully austenitic) have been proposed. First, chemical inhomogeneity due to microsegregation can lead to the enrichment of Ni in interdendritic (-cellular) areas. This enrichment either leads to the formation of austenite already during the late stages of solidification (the first solidification phase expected being ferrite) and/or to a local stabilisation of austenite (that had been formed by solid-state transformation from ferrite) by reducing the M_f temperature to values below the room temperature [86]. Next, the small solidification cell size (2 µm or less in diameter) and the residual stress in the material can hinder the martensitic transformation [87]. Finally, the austenite is stabilized by the uptake of nitrogen into the solid solution during processing (see next section). While all of these explanations are plausible, there is no consensus yet in the literature about the solidification and solid-state phase transformation paths in L-PBF produced 17–4 PH.

In one study, the as L-PBF produced sample consists predominantly of coarse BCC ferrite phase, with only 10.5% of smaller austenite and martensite grains at the melt pool boundaries [85]. The authors speculate that the fine-grain austenite/martensite structures are formed in the heat affected zone at the melt pool boundaries, where the intrinsic heat treatment (re-heating by subsequent scan tracks and layers) induces local recrystallization and phase transformation. They do not discuss the reason for the majority phase being ferrite, but it stands to reason that the material solidified as ferrite and never transformed to austenite during cooldown [85].

4.3. Effect of atomizing media and L-PBF process atmosphere on phase selection in PH stainless steels

Several studies investigated the effect of atomizing medium on the powder properties and final microstructure of 17–4 PH [79,80,89,90]. Atomization can be performed either by water [79,90], or by different gases, such as Ar or N_2. It has been shown that powders atomized using Ar gas are completely martensitic, while N_2-atomized powders are primarily austenitic, with ~6% martensite phase [91] (cf. the micrographs and XRD diffractograms in Fig. 14). This difference in the phase content is attributed to the 40% higher thermal conductivity of N_2 gas, causing a faster cooling during atomization compared to Ar [91]. However, using N_2 as atomizing medium could also incorporate additional nitrogen, which has an austenite-stabilising effect, into the material and thus affect the final microstructure. Unfortunately, these studies do not report the N_2 composition in the as-atomized powder [79,91].

The effect of L-PBF chamber gas (Ar or N_2) on the microstructure of 17–4 PH steels has been evaluated [87,89]. For an Ar gas atomized powder, a martensitic microstructure in the as-fabricated samples was obtained regardless of the process gas atmosphere. In samples produced using N_2 gas atomized powder, the atmosphere during L-PBF had a strong impact on the phases present after the process: under an N_2 atmosphere, the resulting microstructure was 50–75% austenite, while under an Ar atmosphere the microstructure was only ~8% austenite [87].

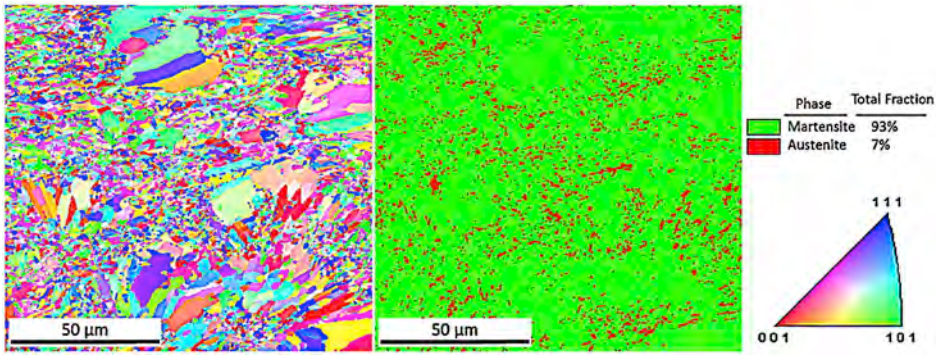

Fig. 12. EBSD inverse pole figure map (left) and phase map (right) of 17–4 PH stainless steel produced by L-PBF. The high fraction of retained austenite, stabilized by the very small austenite grain size is visible. Note the bimodal grain size distribution in this specimen. Adapted with permission from Ref. [88].

4.4. Effect of L-PBD process parameters on phase content in PH stainless steels

The high variance in the reported as-produced microstructures for this material suggests that the laser melting parameters during L-PBF have a marked influence on the amount of retained austenite obtained after building. It was shown that the austenite fraction could be changed merely by changing the laser scan strategy in L-PBF. In samples produced with a concentric-type scan strategy (outside-in succession of concentric rings), the austenite content was much higher (82%) compared to regular scan strategies (~50%) [93]. This is attributed to different thermal gradients in the sample depending on scan strategy [93]. Changing the volumetric energy density also has an effect on the austenite fraction [75].

4.5. Post-heat treatment studies of PH stainless steels: homogenization and Cu precipitation

Sun et al. [85] have performed a microstructure comparison of wrought and AM produced 17–4 PH steels in the as-produced, solution heat treated and aged states. They show that a solution heat treatment (4h at 1038 °C) with final quenching leads to a fully martensitic microstructure also in L-PBF produced material. Fig. 13 shows TEM micrographs of 17–4 PH produced by L-PBF and conventionally. Both samples have been solutionized and aged (1h at 482 °C). Apparently, the differences in the initial microstructure of wrought and AM specimens have no significant effect on the Cu precipitation during ageing heat treatment. Other studies also show that heat treatment can transform AM-produced 17-4 PH steel microstructures to be very similar to the ones expected from wrought material [87,88]. Merely ageing as-produced material (at temperatures between 495 and 620 °C) also decreases the retained austenite fraction, but not beyond ~20% [80]. Lass et al. [94] investigate a number of heat treatment schedules and propose an alternative multi-step heat treatment and quenching process to obtain a suitable "condition A" microstructure of 95% martensite and 5% retained austenite. This heat treatment includes a low-temperature treatment at −60 to 0 °C in order to induce martensite transformation.

4.6. Hardness and tensile test properties of PH stainless steels

The different fractions of martensite and austenite in 17–4 PH steel impact the mechanical properties not only due to austenite being a softer phase, but also because the precipitation reaction during ageing occurs only in martensite. Therefore, a large range of values for mechanical properties such as hardness [80,89,95], yield and ultimate tensile strength, and elongation at fracture have been reported, dependent on the microstructure of the material. In the as-produced state and the as-produced and age hardened state, the material is typically softer and less strong than wrought and age hardened material [96].

The different microstructural states are also reflected in the tensile test response of 17–4 PH steel. Fig. 15 shows the stress-strain curves of as-produced material as well as solutionized, solutionized and aged, and direct aged material [87]. In the as-produced material processed under nitrogen atmosphere, when the microstructure contains >50% retained

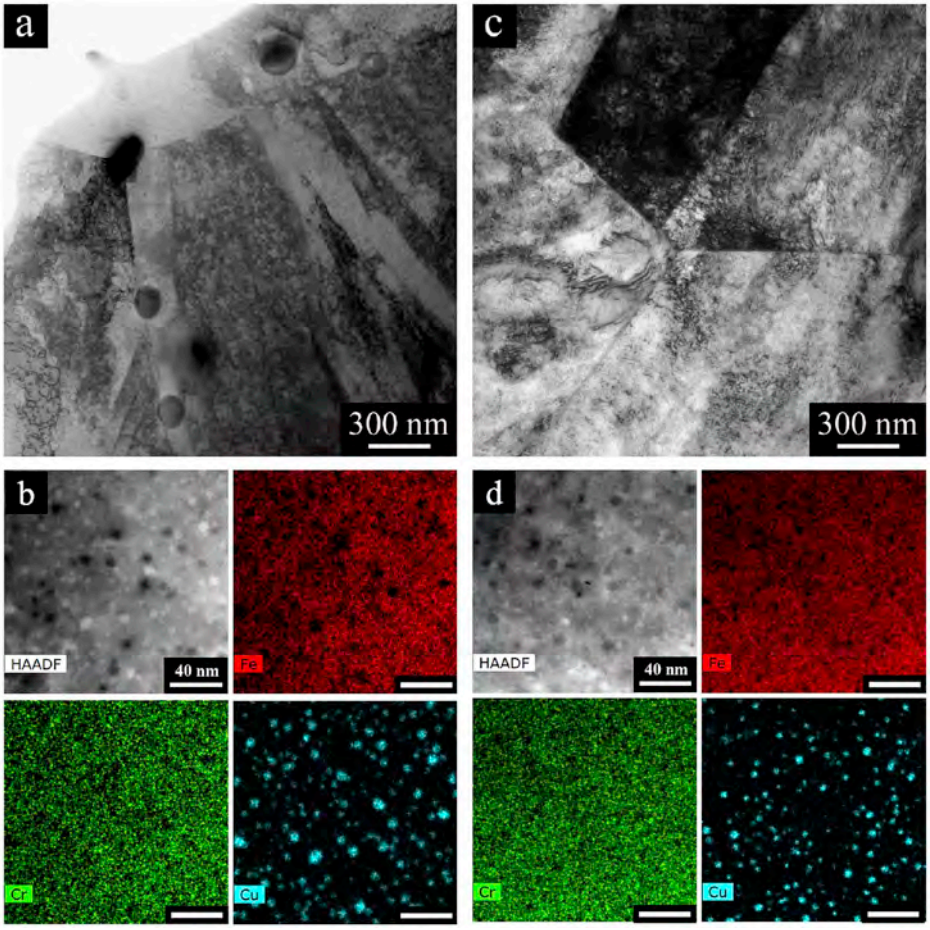

Fig. 13. STEM micrograph of solution heat treated and aged 17-4 PH steel produced by L-PBF (a, b) and conventionally (c, d). (a) and (c) lower magnification HAADF images; (b) and (d) higher magnification EDS maps showing Cu-rich precipitates (all scale bars are 40 nm). Solution heat treatment largely eliminates the differences between the processing routes and precipitation is similar in both specimens. Adapted with permission from Ref. [85].

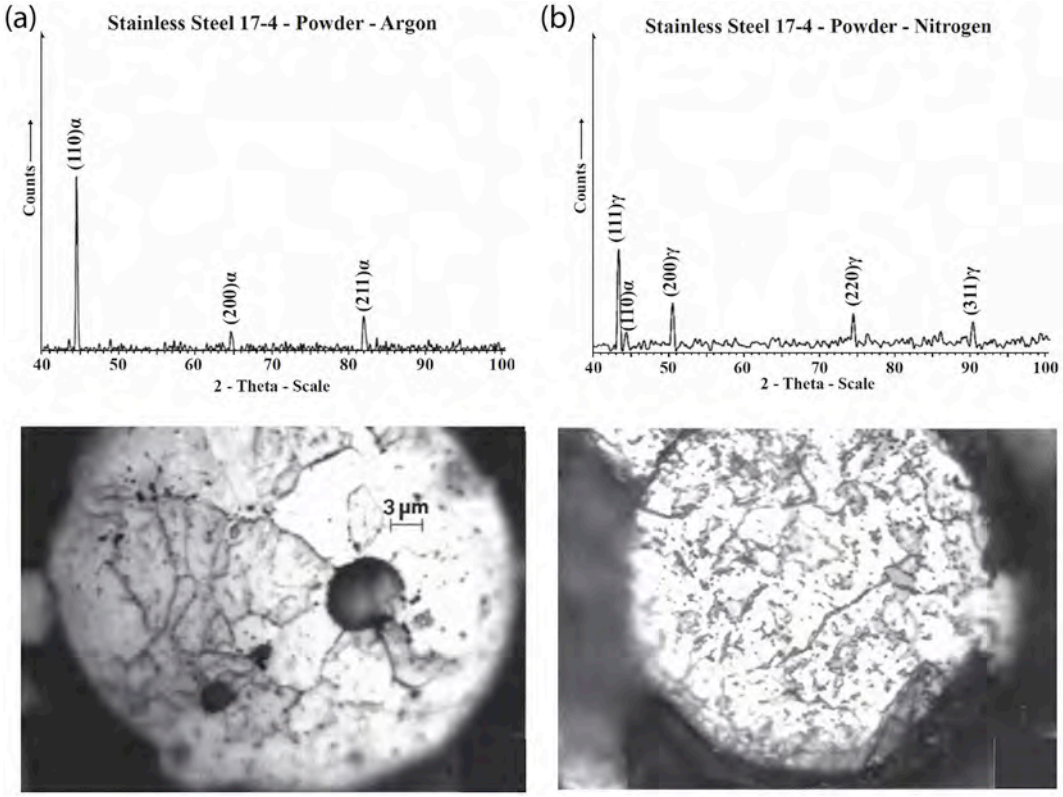

Fig. 14. Microstructures and corresponding XRD measurements of (a) Ar-atomized and (b) N_2-atomized 17–4 PH stainless steel powders. Reprinted under Creative Commons license (CC BY-NC-ND 4.0) from Ref. [92].

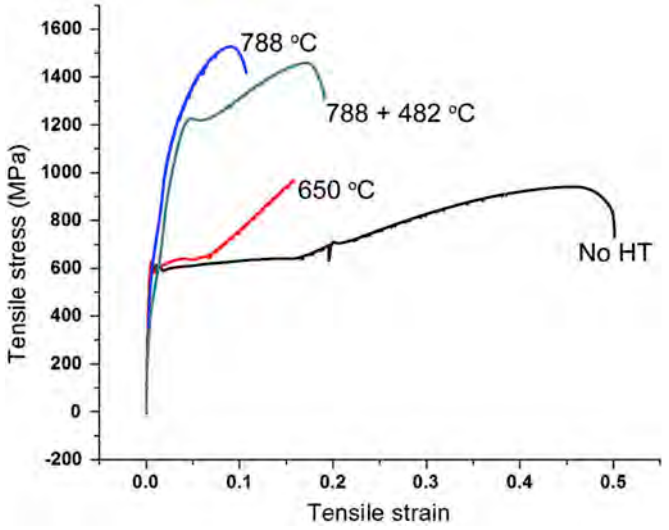

Fig. 15. Tensile test results for 17–4 PH stainless steel produced by L-PBF in various heat treatment states. "No HT": as-produced state, all other heat treatments performed for 2h at the temperatures indicated (1h at 482 °C). In the as-produced state, the high fraction of retained austenite leads to a pronounced TRIP effect, while heat treatment at 788 °C leads to a fully martensitic microstructure with increased strength. Reprinted with permission from Ref. [87].

austenite, strain-induced martensite formation during the tensile test occurs (TRIP effect) as evidenced by the low strain hardening rate in the early stage of plastic deformation. The measured elongation to fracture is just under 50% and the yield strength is 600 MPa. Compared to fully age hardened wrought material, the former is very high, while the latter is quite low. Imposing a solutionizing treatment transforms the retained austenite to martensite and consequently the yield strength increases strongly at the cost of a reduced elongation at fracture. As is the case for other AM-produced steels, given the correct heat treatment, the strength of the material can be as good as or even surpassing conventionally-produced material, but typically at slightly lower ductility [94,97]. "Correct heat treatment" in the case of PH steels refers to a treatment that aims to transform the retained austenite to martensite, with subsequent ageing.

4.7. Fatigue properties of PH stainless steels

AM induced defects in the microstructure such as voids, oxides and un-melted particles, as well as surface defects such as enhanced surface roughness affect the material's fatigue behaviour under cyclic loading [98,99]. Additionally, due to the AM-typical crystallographic texture and the anisotropic distribution of process defects, both low-cycle and high-cycle fatigue properties of L-PBF produced 17–4 PH are dependent on the build orientation [88,100]. Samples tested parallel to the build direction showed a shorter fatigue life compared to samples tested perpendicular to the build direction. This is due to the morphology of build defects (unmelted areas, lack-of-bonding defects) that leads to a higher defect area per gauge area in the direction parallel to the build direction compared to perpendicular to the build direction. These internal defects serve as crack initiation sites.

Interestingly, heat treating the material (solutionizing and ageing) does not improve the fatigue life under all conditions [88]. At high strain amplitudes, when fatigue life is short, the impact of defects is less strong than at low strain amplitudes and long fatigue life. Since defects dominate the mechanical behaviour of the strong, heat treated material more than that of that of the softer, as-produced material, the former shows a higher fatigue strength in the low-cycle regime and vice versa (see Fig. 16) [88].

To our knowledge, no detailed investigations about the fatigue behaviour of DED- and E-PBF-produced PH stainless steels exist in the literature.

4.8. Corrosion resistance of PH stainless steels

L-PBF produced 17–4 PH steel shows a better resistance to corrosion compared to wrought 17–4 PH. This result was found for both gas- and water-atomized powder (type of gas not specified), and only applies when the material shows full relative density [101]. Both the polarization resistance [90] as well as the pitting potential [102] (cf. Fig. 17) are improved compared to wrought material (both materials solutionized and aged). The better corrosion resistance is attributed to the refined microstructure of AM-produced material (both finer lath martensite and finer, homogenously distributed NbC precipitates) and the increased stability of the passive film as a result of an increased nitrogen content in the AM-produced material stemming from N_2 gas atomization [102].

4.9. PH stainless steels: other AM processes

A recent study showed the feasibility of wire and arc additive manufacturing (WAAM) of 17–4 PH steels [86]. The as-deposited WAAM 17–4 PH microstructure had a dense δ-ferritic/martensitic microstructure with a small amount of retained austenite. The presence of 38% helium in the argon-rich shielding gas reduced the amount of retained austenite. The authors state that a higher heat input and therefore a slower cooling rate is expected when using He shielding gas compared to Ar, due to the higher thermal conductivity of He. Also in this study, solutionizing and ageing leads to a microstructure comparable with wrought material and satisfactory mechanical properties [86]. 17–4 PH steel has been successfully produced by DED, but reports in the literature are very scarce until now [103,104].

4.10. AM of 15-5 PH grade stainless steel

Several studies focused on the feasibility of manufacturing 15–5 PH steels using L-PBF and investigated the effect of build orientation on its high-temperature tensile and fatigue properties [53,105–109]. Roberts et al. [110] reported a completely martensitic 15–5 PH steel having a 30% higher tensile strength at 593 °C and 50% higher Vickers hardness at room temperature than wrought 15–5 PH. Stress rupture tests at 593 °C and 211 MPa showed that AM 15–5 PH had a ~30% higher rupture life than conventional 15–5 PH [110]. However, the mechanisms for this creep life improvement has not been clarified yet.

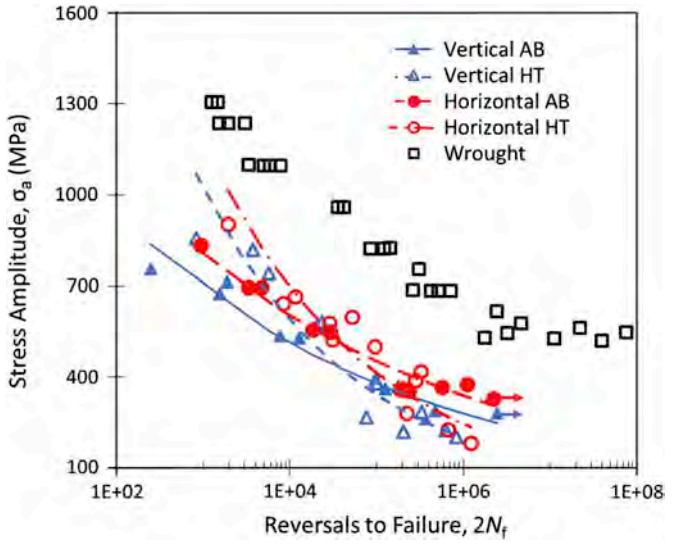

Fig. 16. Fully reversed fatigue test results for 17–4 PH steel produced by L-PBF, compared with conventionally produced material. "AB": as-built, "HT": heat treated (solution heat treated and aged). Specimens were built in two different directions (specimen long axis along build direction: "vertical", perpendicular to build direction: "horizontal"). Although heat treatment improves the stress life of AM-produced specimens, their fatigue performance lags behind conventionally-produced material due to the presence of defects in the microstructure. Reprinted with permission from Ref. [88].

4.11. Martensitic stainless steels

There is very limited information available on the processing of martensitic stainless steel. The only grade in use so far seems to be 420 (1.4021, X20Cr13). It is possible to obtain fully dense specimens with fully martensitic microstructures both by DED [111,112] and by L-PBF [113]. The phase content of the microstructure depends strongly on the chosen process parameters: DED processing can result in a mixture of martensite and eutectic (δ-) ferrite, while L-PBF processing under high laser power can result in retained austenite as well. The former duplex microstructure results in a higher hardness compared to conventional processing [112], while the latter results in hardness comparable with wrought material (up to 51 HRC) [113].

5. Martensitic microstructure: Tool steels

There are two kinds of tool steels in use in AM, namely carbon-free maraging steels and carbon-bearing tool steels. In both kinds of tool steel, the final microstructure in use consists of martensite with precipitates. However, in the case of carbon-bearing tool steels, the martensitic matrix without precipitates obtained upon quenching is hard and brittle and tempering serves to regain some ductility by precipitating carbon from the martensite matrix in the form of carbides. In the case of the high-Ni maraging steels, on the other hand, quenching leads to a comparably soft and ductile martensitic microstructure which gains its strength by precipitation of intermetallic-phase particles upon ageing [114,115]. Since the cooling rates in fusion AM processes are

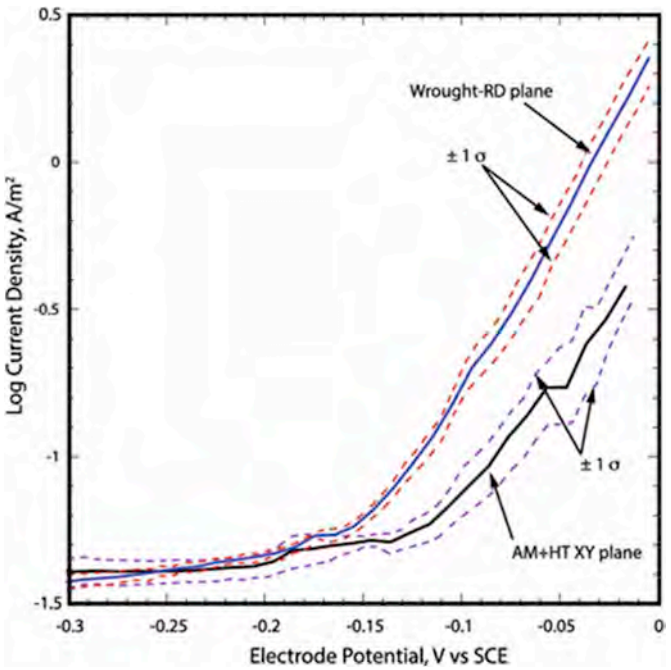

Fig. 17. Onset of pitting corrosion in wrought and heat treated, L-PBF-produced 17–4 PH stainless steel. The steep rise in current density, signifying pitting corrosion, occurs at higher electrode potentials in AM-produced material compared to conventionally-produced material Reprinted with permission from Ref. [56].

typically high, martensite formation is induced in both kind of tool steels during AM. Therefore, maraging steels with a ductile martensitic microstructure are well processable in AM while carbon-bearing tool steels with a brittle martensitic microstructure tend to crack a result of thermal stresses built up during the AM process [116]. A considerable fraction of the literature on carbon-bearing tool steels is therefore concerned with finding the optimum process parameters to produce crack free, dense samples. In contrast, for maraging steels most studies are aimed at optimizing microstructures, mechanical properties and post process heat treatments.

5.1. Maraging steels

5.1.1. The microstructure of as-built maraging steels

For maraging steels, the most widely used alloy in AM is 18Ni-300 (1.2709, X3NiCoMoTi 18-9-5) [1,9,114,117–133]. There are only a few examples of other types of maraging steels in the AM literature, such as 18Ni-250 (1.6359 (~1.2706), X2NiCoMo18-8-5) [134], 14Ni-200 [135,136] as well a Fe–Ni–Al maraging-type model alloy [137]. In the remainder, we therefore focus the discussion on the 18Ni-300 grade.

Crack free samples with relative densities above 99% can be readily produced [114,119,123,126,127,131]. Compared to conventionally produced (wrought) maraging steels which are almost fully martensitic [130,138], AM produced maraging steels show a drastically different microstructure. They have a cellular/dendritic solidification microstructure in L-PBF [1,114,119,120,122,123,125–127,130–132] (see Fig. 18) as well as in DED [128,130,137] with cell sizes of approximately 0.3–2 μm in L-PBF and around 5 μm in DED. The prior austenite grains are relatively coarse with grains up to 1 mm in diameter in DED-produced material. Within this solidification microstructure, the martensitic phase transformation occurs. The resulting microstructure looks rather different from conventionally-produced maraging steels: the blocks of martensite laths are mainly found within the individual solidification cells as they are often (yet not always) confined by retained austenite along cell boundaries [130]. The retained austenite is a consequence of the enrichment of alloying elements in the interdendritic (intercellular) region by microsegregation during solidification (cf. EBSD and EDS maps in Fig. 19). The enrichment of Ni stabilizes the austenite to room temperature [130,137]. Therefore, AM produced maraging steels contain a significant amount of austenite (6–11%, depending on processing conditions) [120,122,129–131].

5.1.2. The texture of as-built maraging steels

The retained austenite grains show a fibre texture with the crystallographic <001> orientation parallel to the build direction [139]. As in other steels, this is attributed to the preferential growth during solidification along the maximum thermal gradient [4]. Unlike in e.g. austenitic stainless steels, the solid state martensite transformation in maraging steels leads to a pronounced weakening of the texture, because one austenite grain orientation leads to a multitude of martensite variants and hence possible crystallographic orientations [114,139]. Fig. 20 shows the resulting almost random grain orientation with no specific texture noticeable in either an EBSD mapping or in the corresponding pole figures.

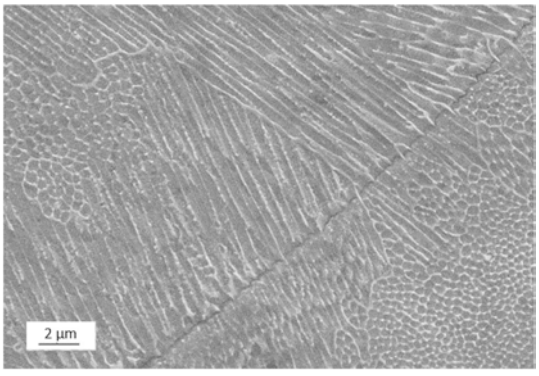

Fig. 18. SEM micrograph showing the cellular/dendritic solidification microstructure of L-PBF produced 18Ni-300 Maraging steel. Reprinted under Creative Commons license (CC BY 4.0) from Ref. [129].

5.1.3. Heat treatment of maraging steels

The cellular microstructure is retained upon aging at common aging temperatures (490–530 °C) [114,120,124,133]. At higher aging temperatures such as 600 °C, substantial austenite reversion takes place [133]. The cellular microstructure completely disappears after solution treatment (usually between 815 and 840 °C, where the steel is fully austenitic) [119,120,123,125,129] and is replaced by a fully martensitic yet coarser microstructure upon quenching [120,129]. This leads to a decrease in hardness and strength compared to the as-produced state [119,125,129].

As mentioned before, the reason for the outstanding combination of strength and toughness of maraging steels is the hardening of the martensitic microstructure by intermetallic precipitates during the aging heat treatment. In the as-L-PBF-produced condition, no precipitates or small clusters of atoms are found in 18Ni-300 [114,122,124,130], indicating a cooling rate high enough to suppress precipitation. However, there are indications for early stages of precipitation in DED-produced material, accompanied by an increased hardness [130]. This is shown to be the result of repeated re-heating of the material upon deposition of additional tracks and layers, a condition termed intrinsic heat treatment (IHT). A simple ternary Fe–Ni–Al maraging model alloy, specifically designed to show precipitation upon IHT during DED processing, shows a high number density of intermetallic NiAl precipitates directly after AM without additional ageing post-heat treatment [137].

The precipitation sequence upon post-AM-process aging heat treatment of L-PBF-produced maraging samples is comparable to conventionally produced maraging steels [115,140,141]: first, spherical Ni_3X precipitates (η-phase) are formed with X being Ti, Al, Mo [114,119,122,124,130] followed by Fe_7Mo_6 (μ-phase) precipitates [122,124,130](cf. Fig. 21). See Ref. [130] for a comparison of precipitation in conventional, L-PBF- and DED-produced material.

5.1.4. Tensile mechanical properties of maraging steels

Overall, the mechanical properties of AM-produced maraging steel are comparable to conventionally produced material, but not entirely identical. Material produced by L-PBF displays equal or slightly higher yield and ultimate tensile strength compared to conventionally produced material in the non-aged condition despite the finer microstructure resulting from L-PBF [119,120,123,131]. After an aging heat treatment (both with and without prior solutionizing), a significant increase in hardness (e.g. from 381 to 645 HV) and in tensile strength accompanied by a reduction in ductility is observed, as expected [119,125,129,131].

Together with precipitation, austenite reversion is observed at the cell boundaries around retained austenite during ageing [120,122,129,131]. In conventional material, no austenite, neither retained nor reverted, was observed, which is the reason for its higher hardness compared to AM produced material in the aged condition [130]. Upon aging heat treatment the toughness reduces significantly and in the aged condition it is lower for L-PBF produced material compared to conventionally produced one [114,119,131]. Tan et al. found the mechanical properties to be isotropic [114].

Casati et al. concluded that a solution treatment of L-PBF prduced samples is not necessary and consequently the as-prduced samples can be directly aged [129]. In Fig. 22, the results of their tensile tests before and after ageing are shown. They found that the retained austenite does not play a key role in the fracture process and that the reversion of austenite plays a minor role compared to the strengthening effect of the intermetallic precipitants. In contrast, Tan et al. [120] argue that after

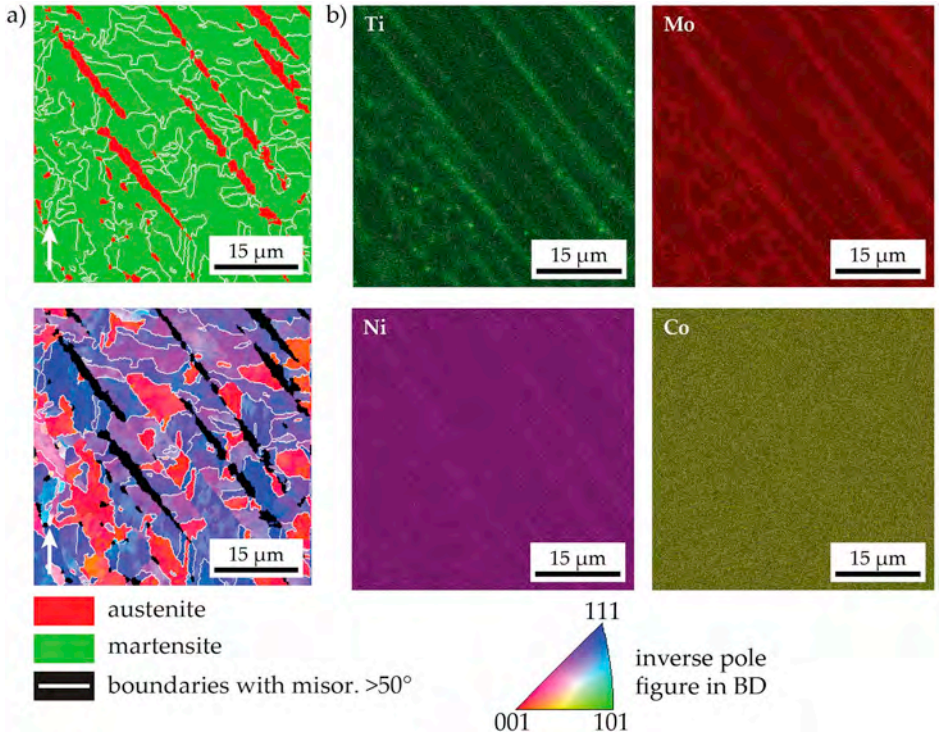

Fig. 19. EBSD mapping (a) together with corresponding EDS element mapping of DED produced 18Ni-300 Maraging steel. The enrichment of alloying elements in the interdendritic (intercellular) regions stabilizes austenite. Reprinted under Creative Commons license (CC BY 4.0) from Ref. [130].

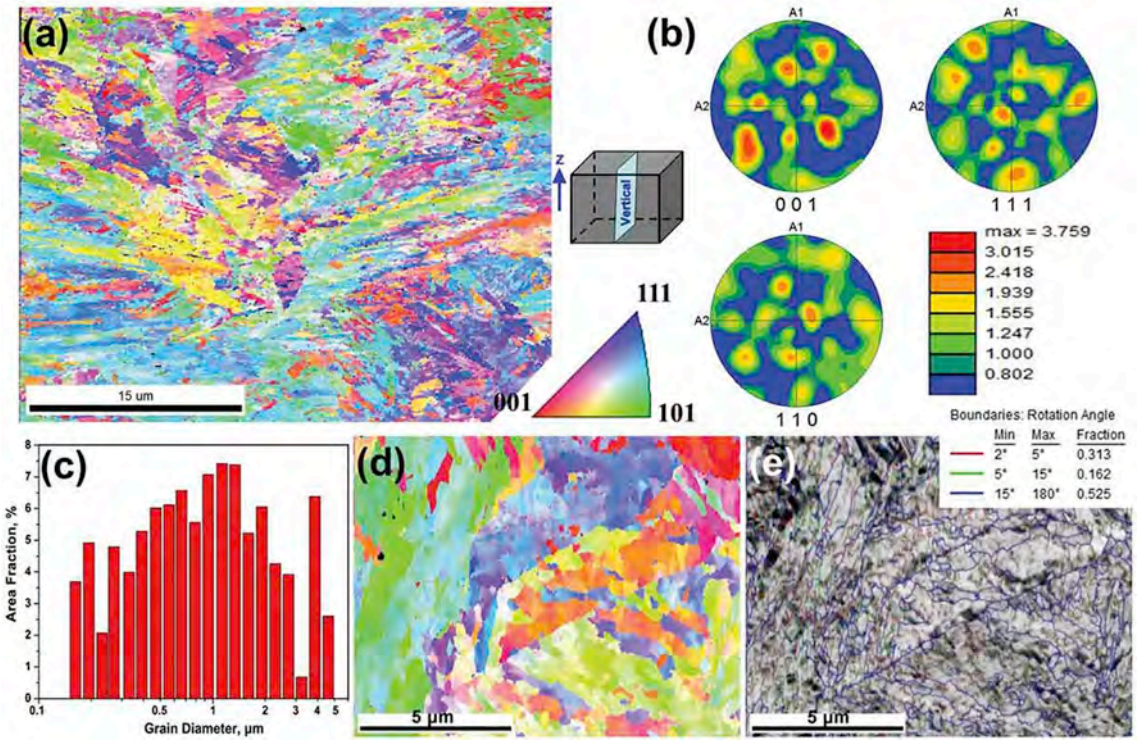

Fig. 20. EBSD analysis of L-PBF produced 18Ni-300 Maraging steel (vertical cross section through the sample). (a) depicts an inverse pole figure colored map. (b) Shows the corresponding pole figures. Reprinted under Creative Commons license (CC BY 4.0) from Ref. [114].

solution and aging heat treatment the fracture mechanism is more favourable than directly aging the as-produced material and suggest that solution treatment should be performed. See Table 2 for an overview of published mechanical properties of 18Ni-300 maraging steel.

5.1.5. Fatigue properties of maraging steels

Croccolo et al. found the fatigue properties to be isotropic with a fatigue limit of 600 MPa [117] (i.e. 1/3 of the static yield strength, in line with results for conventionally-produced maraging steel [142,

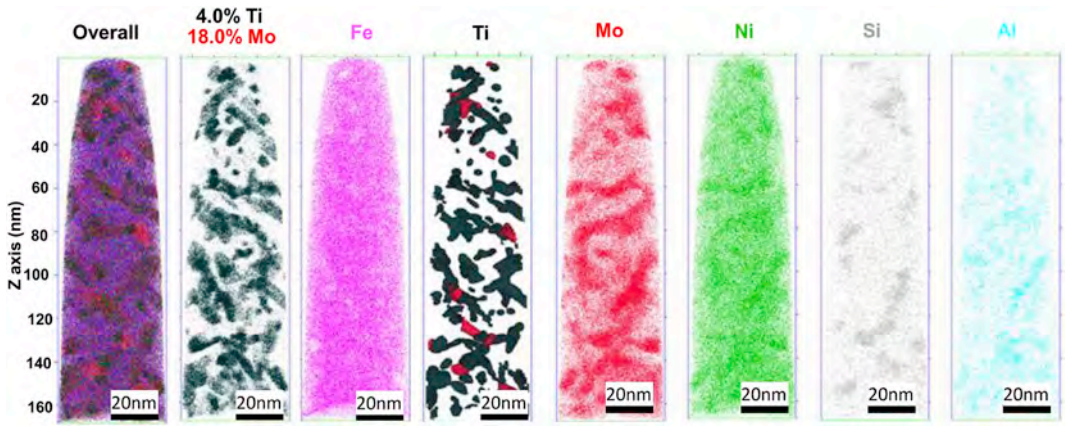

Fig. 21. Atom probe tomography reconstruction showing the different types of precipitates (Ni_3Ti (η type) and Fe_7Mo_6 (μ phase)) occurring in a L-PBF produced 18Ni-300 Maraging steel after aging at 510 °C for 2h. Reprinted with permission from Ref. [124].

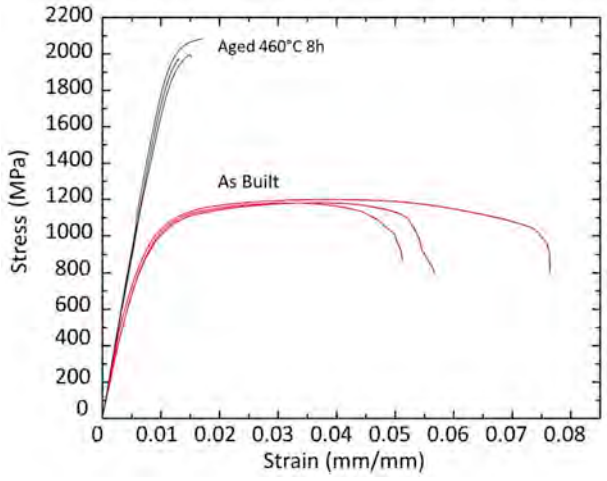

Fig. 22. Tensile curves of L-PBF produced 18Ni-300 maraging steel before and after aging at 460 °C for 8h. Reprinted under Creative Commons Attribution License (CC BY 4.0) from Ref. [129].

143]). Becker et al. found the fatigue crack growth rates of peak aged material to be isotropic and equal to conventionally-produced material [123]. Isotropy is due to the weak texture in this material as a consequence of the martensitic phase transformation, as explained above. Despite virtually defect-free samples, the ductility and fracture behaviour is still strongly affected by the properties of any defects remaining in the material, i.e. their orientation, morphology, arrangement etc. [125,129].

5.2. *Carbon-bearing tool steels*

The most prominent examples of carbon-bearing tool steels used in AM are the high speed steels M2 (1.3343, HS 6-5-2 C) [18,116,144–149] and HS 6-5-3-8 (1.3294, ~M3.2) [150], the cold working steels X65MoCrWV3-2 [151] and the hot working tool steels H11 (1.2343, X38CrMoV5-1) [10,152–157] and H13 (1.2344, X40CrMoV5-1) [11,12,148,158–179,182]. Most articles deal with the tool steel H13 and the phenomena encountered there are representative for the whole class of steels. Therefore, we will first describe the microstructure and mechanical properties of H13 in detail before briefly touching on the other tool steels in use in AM.

Table 2
Overview of published mechanical properties of 18Ni-300 maraging steel. AP: as produced, SA: solution annealed, AH: ageing heat treated.

Source	condition	E (GPa)	$R_{p0.2}$ (MPa)	YS (MPa)	UTS (MPa)	elongation at fracture (%)	Hardness (HV or HRC)	Tough-ness (J)
[120,123,126,131]	Wrought SA	180		760–895	830–1170	6–17	30-37 HRC	
	Wrought AH	183–193		1790–2070	1830–2100	5–11	525 HV/54 HRC	
[119]	L-PBF AP				1178	7.9	381 HV	24
	L-PBF SA				1080	10.2	341 HV	24
	L-PBF AH				2164	2.5	645 HV	5
[123]	L-PBF AP	181		815–1080	1010–1205	8.3–12	420 HV	
	L-PBF SA	161		800	950	13,5	320 HV	
	L-PBF AH	220		1750	1850	5,1	600 HV	
[124]	L-PBF AP						370 HV	
	L-PBF AH						573 HV	
[121]	L-PBF AP		1000		1200	8		
[125]	L-PBF AP		900		1200	6		
	L-PBF AH		1950		2000	1,5	630 HV	
[126]	L-PBF AP				1085–1192	5–8	30-35 HRC	
[127]	L-PBF AP	166		985	1152	7.6	34 HRC	
[129]	L-PBF AP			915	1188	6.1	371 HV	
	L-PBF SA						279 HV	
	L-PBF AH			1957	2017	1.5	600 HV	
[131]	L-PBF AP	163	1214		1290	13,3	40 HRC	42
	L-PBF AH	189	1998		2217	1,6	58 HRC	5
[120]	L-PBF AP			915	1165	12.4	35-36 HRC	
	L-PBF AH			1967	2014	3.3	53-55 HRC	
	L-PBF SA			962	1025	14.4	28-29 HRC	
	L-PBF SA + AH			1882	1943	5.6	52-54 HRC	

5.2.1. Microstructure and texture of carbon-bearing tools steel H13

It was shown that virtually dense and crack free samples from H13 (1.2344, X40CrMoV 5–1) can be produced by DED with optimized process parameters [173,175,176,178]. Dense as well as crack free samples can be achieved by heating the base plate during the L-PBF process to at least 100 °C [12,158,161,170,174]. It has been shown that H13 can be processed by electron beam melting (E-PBF), which requires a pre-heated powder bed in all cases [13,180]. Similar to maraging steels, the microstructure of AM-produced H13 tool steel consists of solidification cells/dendrites with retained austenite located in the interdendritic regions. The cell size ranges from 0.5 to 2 µm for L-PBF [158,162,166,174] and from 2 to 30 µm for DED [165,167,169,173,175]. In DED, the secondary dendrite side arms are more pronounced than in L-PBF [175]. Brooks et al. [177] suggest from WDS measurements that Cr, Mo as well as V are enriched in the interdendritic/austenitic region. As in maraging steel, the cellular structure is the result of microsegregation during solidification which enriches some of the alloying elements in the interdendritic regions. In particular the enrichment of carbon stabilizes the austenite to room temperature (see Fig. 23) [172]. In contrast to maraging steels, however, carbide precipitates can already be present in the as-AM-produced state [158,161,166,169,172–175].

Alternative explanations for the austenite formation have been proposed. Holzweissig et al. hypothesize that the austenite is formed upon carbon diffusion in the solid due to the IHT [158]. Krell et al. propose a delta ferritic solidification of the dendritic region and a gamma solidification of the interdendritic region [174]. It must however be noted that there is no conclusive experimental evidence for these alternative explanations.

There is only limited information available in the literature regarding the texture of H13 tool steel. Probably the crystallographic texture in L-PBF produced material is very weak, for the same reasons as in maraging steels [162].

5.2.2. In-situ and ex-situ heat treatment of carbon-bearing tool steels

Since martensite formation induces transformation strain and turns the material brittle, and since pre-heating the base plate eliminates cracking, an obvious conclusion is to assume that pre-heating prevents martensite formation by keeping the temperature above the martensite start temperature M_S. However, for all pre-heating temperatures up to 300 °C, which is above the M_S temperature for the nominal composition of H13, the same cellular solidification structure and martensitic microstructure is found [174]. This suggests that cracking is avoided due to the lower thermal gradients and reduced residual stresses at elevated temperatures rather than due to a suppression of martensite formation. Base plate heating of 400 °C changes the phase transformation and hence the microstructure after cooldown significantly: by keeping the part above the M_S temperature, a bainitic microstructure is formed [161]. This bainitic sample shows a higher hardness as well as higher tensile strength compared to the martensitic microstructure obtained at lower heating temperatures. It must be noted that authors typically report the nominal base plate temperature, usually measured in the heating itself below the base plate. The actual temperature in the sample being built can be significantly lower than this nominal temperature. Another factor is the chemical inhomogeneity of the material: Due to microsegregation, the steel inside dendrites/cells contains less carbon than the nominal composition and hence locally has a higher M_S temperature.

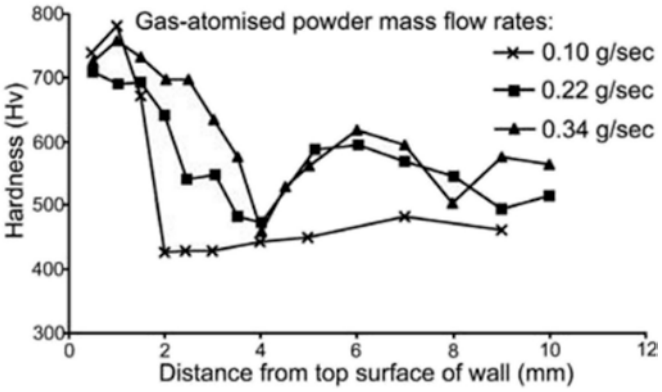

Fig. 24. Hardness profile along the cross section of a DED built H13 tool steel sample. The highest hardness in the top region of the sample (left side of the graph) is due to the fact that here the martensite is untempered. The layers below are tempered by the IHT and therefore softer. The hardness peak at around 6 mm from the top is presumably due to secondary hardening (i.e. precipitation of carbides). Reprinted with permission from Ref. [160].

Like in L-PBF, DED-produced H13 shows a martensitic microstructure with some retained austenite. But unlike L-PBF, the martensite is tempered due to the heat input upon IHT during DED [173]. This effect is visible when comparing the hardness of the top layer (negligible IHT) to lower layers of a sample (significant IHT): in as-DED-produced H13, the top layer has a higher hardness compared to the lower layers (see Fig. 24) [156,160,164,175]. The lower layers tempered by the IHT contain V and Cr rich carbides [177]. These are mainly MC-type carbides, plus a small amount of M_7C_3 carbides [169]. Cottam et al. attribute the transformation of retained austenite to martensite to the in-situ tempering due to the IHT [179]. During the build, also the cooling rate during solidification decreases as the part becomes taller and heat conduction into the base plate is reduced. Therefore, solidification cell

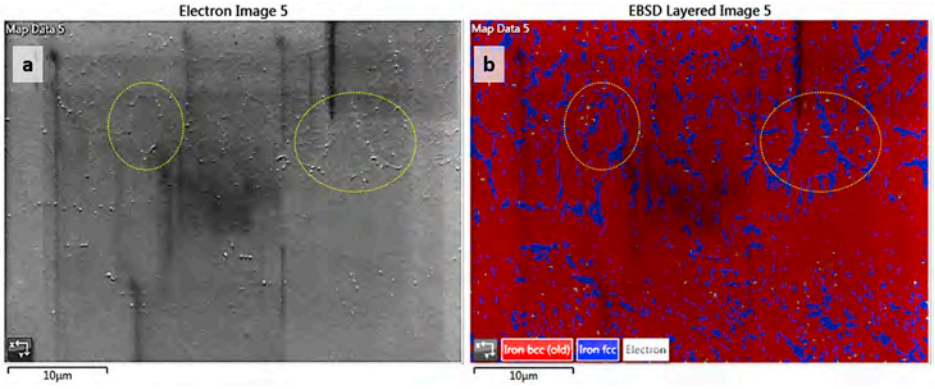

Fig. 23. SEM micrograph (a) together with the corresponding EBSD analysis (b) of H13 steel built by L-PBF. The main microstructure constituent is martensite (red). Austenite (blue) is stabilized at the cell boundaries due to microsegregation. Reprinted with permission from Ref. [172]. (For interpretation of the references to colour in this figure legend, the reader is referred to the Web version of this article.)

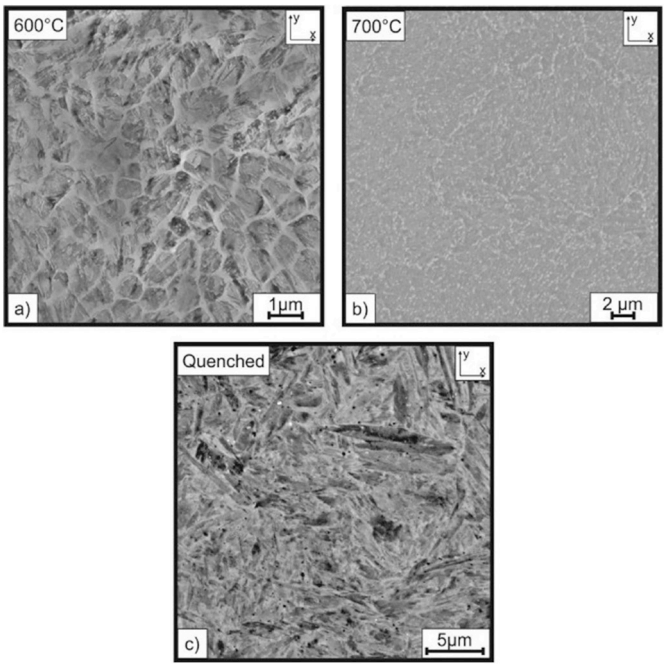

Fig. 25. SEM micrographs showing the microstructure of H13 steel samples produced by L-PBF at 200 °C pre-heating temperature after different heat treatments: a) and b) tempering at 600 °C and 700 °C respectively. C) austenitization at 1040 °C followed by oil quenching. Reprinted with permission from Ref. [174].

diameters at the top of the build are larger compared to the bottom of the build [178].

A similar in-situ tempering effect by the IHT as in DED has also been reported for L-PBF [161,172]. However, the results are not as conclusive as in the case of DED-produced material: Zheng et al. found Fe_3C cementite (as well as retained austenite) in the martensitic microstructure in the as-L-PBF produced state by means of XRD [166], while Ren et al. did not find any precipitates by TEM [162]. Both studies do not mention the use of base plate heating. Deirmina et al. find precipitation of transition carbides, followed by M_3C, $M_{23}C_6$ carbides and finally MC, M_2C and M_6C upon tempering of an austenitized and quenched L-PBF-produced sample in a dilatometer. Since the first two precipitation reactions are not observed upon tempering of an as-produced sample, they propose that a low-temperature transformation already occurs during the L-PBF process [172]. Mertens et al. attribute the higher hardness in the top layer compared to the bulk of the sample to a tempering of the martensitic microstructure for builds without and with base plate heating up to 200 °C [161].

The retained austenite decomposes during post-heat treatment at 500 °C, and the cellular solidification microstructure disappears at tempering temperatures above 600–700 °C [172–174]. Complete austenitization followed by quenching results in a martensitic microstructure very similar to conventionally produced material without retained austenite [171–174] (see Fig. 25).

L-PBF produced samples that are tempered directly from the as-produced state do not show the dip in hardness at low tempering temperatures that is characteristic for conventionally produced material and that is due to softening of the martensite [172,174]. Furthermore, the secondary hardness peak is shifted to significantly higher temperatures. This can be explained by a high amount of carbon and carbide formers being bound in the retained austenite that is stable up to relatively high temperatures [172–174]. Only when this austenite is decomposed, the secondary carbides can form.

5.2.3. Mechanical properties of carbon-bearing tools steel H13

Reported hardness values in the as-L-PBF produced state range from 570HV up to 680HV (and even 745HV in the skin area [163]) [162,170,174]. These values are similar to or even higher than as-quenched (hardened) wrought H13 material, reflecting the fully-martensitic state of this material. The fact that many of the reported values for the yield strength and UTS are significantly lower in the as-L-PBF-built condition than conventionally produced and heat treated H13 suggests that the extreme brittleness of this state leads to premature fracture of tensile test specimens [12,158,161,163,170]. After tempering, the L-PBF-produced material shows almost the same value as wrought and heat treated material [12]. However, the elongation to fracture is much lower in the L-PBF-produced samples in the as-produced as well as aged conditions [12,158,161,163,170], presumably because of remaining process-induced defects such as porosity. For as-DED-produced material, the hardness (550HV to 660HV [164,175,179]), the UTS (~2000 MPa) and the elongation at fracture (5–6%) are similar to those of quenched and tempered wrought material, reflecting its in-situ tempered state [169]. Depending on the application, this could be a desired outcome, since it could alleviate the need for a post-tempering treatment. See Table 3 for an overview of published mechanical properties of H13 tool steel.

The fatigue life of L-PBF produced H13 (as-built surfaces) is significantly below that of conventionally produced material [12]. This can be attributed to the residual stress and the sample surface roughness stemming from the L-PBF process [170]. Even after surface machining the fatigue strength remained significantly lower than that of reference material (50% failure probability at 10^7 cycles strength of 283 MPa compared to 600 MPa) [170]. The fatigue properties drastically improve upon stress relief and austenite decomposition heat treatment at 600 °C [12].

The wear resistance of DED produced H13 is comparable or even superior to that of conventionally produced material [169,181]. The wear loss in a sliding wear pin-on-disc experiment of as-DED produced material was only 1/3 of that of wrought and hardened H13 steel [169]. There is no conclusive information yet available on the wear performance of L-PBF produced H13 steel.

5.2.4. Other carbon-bearing tool steels

The microstructure and processing of H11 (1.2343, X38CrMoV 5–1) produced by L-PBF is similar to the one described for H13 [153–157]. There is as much as 15 wt% retained austenite in the as-produced state, which reduces to 3 wt% or less upon tempering [153,157]. The microstructure also includes a very low volume fraction of M_3C carbides in the as-produced state and $M_{23}C_6$ in the tempered state [153]. A high (nominal) preheating temperature of 500 °C leads to austenite transformation to upper bainite instead of martensite [157].

For M2 steel it was shown that it is possible to produce dense and crack free 1D single line tracks [183] as well as 2D surfaces in L-PBF without pre-heating [184]. 3D structures, however, require base plate heating to at least 200 °C [116,144–147,184]. The microstructure is somewhat different from H11 and H13: microsegregation during solidification not only stabilizes austenite, but also leads to the formation of carbides and possibly eutectic structures in the interdendritic regions [144,148,149,184] (see Fig. 26). The hardness of as-L-PBF-produced M2 steel parts is, at 57 HRC, almost as high as that of heat treated conventionally produced material (65 HRC) [116]. By re-melting each layer during the L-PBF process, the as-produced hardness can even reach values as high as 64 HRC [116]. The tensile testing results of as-produced L-PBF samples are somewhat worse than those of heat treated conventional material, with 1300 MPa UTS and 0.7% elongation at fracture compared to 1600 MPa and 1.5% [116].

There are scattered examples of other, higher-carbon tool steels being processed by AM in the literature. They include high-carbon steel HS 6-5-3-8 (1.3294) [150], X65MoCrWV3-2 [151] and a steel containing even 2 wt% C [185]. These steels can be produced fully dense and

Table 3
Overview of published mechanical properties of H13. AP: As-produced, AH: age hardened (tempered), BP: Base plate temperature during build.

Source	condition	E (GPa)	YS (MPa)	UTS (MPa)	elongation at fracture (%)	Hardness (HV or HRC)
[12,161,164,169]	H13 wrought AH	210	1569–1650	1930–1990	9–12	40-53 HRC
	H13 wrought AP					50-54 HRC
[163]	L-PBF AP			1000–1200	0.8–1.9	612 (skin 745)
[158]	L-PBF AP 100 °C		1150–1275	1550–1650	1.5–2.25	
[164]	DED AP					46-54 HRC
[161]	L-PBF AP RT	190	1236	1712	4.1	
	L-PBF AP (BP 200 °C)	188	835	1620	4.1	
	L-PBF AP (BP 400 °C)	194	1073	1965	3.7	
[12]	L-PBF AP		1003	1370	1.7	59 HRC
	L-PBF AH		1580	1860	2.2	51 HRC
[175]	DED AP					550 (up to 700 in top layer) HV
[160]	DED AP					400-600 (750 in top layer) HV
[165]	DED AP					53-56 HRC
[166]	L-PBF AP					57 HRC
[169]	DED AP		1288–1564	2033–2064	5–6	660
[170]	L-PBF AP (BP 240 °C)	198	892	1440	1.5	571-579 HV

crack free by high pre-heating temperatures (e.g. 500 °C). The solidification microstructure and in-situ tempering is in principle similar to the behaviour described for lower-carbon tool steels above.

6. Ferritic microstructure: ODS steels

Oxide dispersion strengthened (ODS) steels are stainless steels meant for use at high temperatures. They contain a minimum of 12% Cr and essentially no austenite stabilisers, and hence are either martensitic, martensitic/ferritic, or fully ferritic at room temperature. Grades with high Cr contents and with other ferrite stabilising elements are ferritic at all temperatures up to melting. ODS steels achieve their corrosion resistance by their Cr content (as much as 23%) as well as, for some grades, Al additions. Their creep resistance is provided by a homogeneous dispersion of fine oxide particles, typically a few to a few tens of nm in size. With some exceptions, the oxide added is Y_2O_3, although this stoichiometry may change during processing to $Y_2Ti_2O_7$ or other compounds. Additionally, their microstructure makes them attractive in fission and fusion power plants. ODS steels are conventionally produced via a powder metallurgical process route involving mechanical alloying (i.e. prolonged high-energy milling) of metal and oxide powders and hot compaction (e.g. hot extrusion or HIP), potentially followed by post-heat treatments. They are often considered difficult to weld, because the small oxide precipitates may coarsen or leave the weldment during joining.

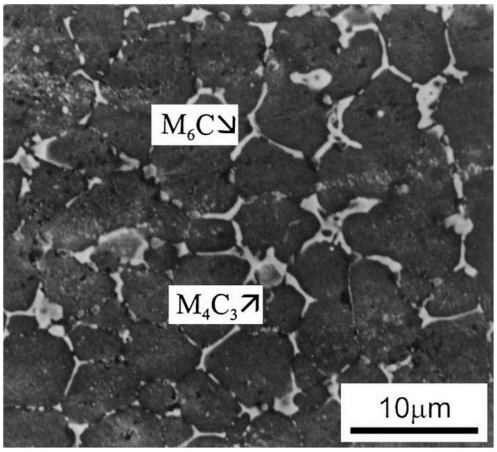

Fig. 26. SEM micrograph of the microstructure of an L-PBF produced M2 steel showing examples of the carbides formed at the cell boundaries. Reprinted with permission from Ref. [186].

6.1. ODS steels by AM of mechanically alloyed powders

Most reports of the use of ODS steels in AM are related to the commercial alloy PM2000 (Fe–19Cr-5.5Al-0.5Ti-0.3Y_2O_3) or its close relative, MA956. The first report of L-PBF processing of an ODS steel is by Walker et al. [187]. They synthesized single-wall specimens from mechanically-alloyed PM2000 powder and showed that a homogeneous distribution of oxides can be retained in this process route. Although the average sizes of the oxides in their samples are somewhat coarser than in conventionally-produced PM2000 (average diameter 48–61 nm by L-PBF, depending on process parameters, vs. 30 nm conventionally), the general feasibility of ODS processing by AM was proven. Processing in this study suffers from a very low available laser power of only 50W, necessitating very slow scanning speeds for full consolidation. The authors show that the slow scanning speed is the main factor contributing to oxide coarsening during the L-PBF process [187].

Subsequent studies use similar processing routes, i.e. melting of fully mechanically alloyed PM2000 or MA956 powders by L-PBF [188–190]. The microstructure in all cases is similar. It is fully ferritic, shows a strong fibre texture with the <001> direction parallel to the build direction, and includes a homogeneous distribution of fine oxides (see Fig. 27). In some cases, also coarser oxides are observed [188], potentially due to agglomeration of nanometre-sized oxides [190]. The crystal structure of the oxides is sometimes reported as $Y_2Ti_2O_7$, sometimes as $Y_4Al_2O_9$ [189]. The strong crystallographic texture leads to an anisotropic mechanical behaviour, with e.g. ductile fracture when strained in the build direction, but brittle transgranular fracture when strained perpendicular to the build direction [188]. After an additional heat treatment, the tensile strength reaches the values of conventionally produced material [188].

Vasquez et al. processed Fe–14Cr–1W powder mechanically alloyed with Y_2O_3 and TiH_2 by L-PBF and report a microstructure of the built parts similar to the one described above for PM2000 [191]. Gao et al. successfully produced mechanically alloyed Fe–18Cr–2W–0.5 Ti–0.3Y_2O_3 powder by E-PBF [192]. They show the preferential arrangement of a part of the small oxides along grain boundaries, 10–40 nm in diameter. The results of tensile tests conducted on the as-built parts at temperatures up to 600 °C, while dependent on the testing direction, are very promising. This includes occurrence of a ductile fracture mode [192].

6.2. ODS steels synthesized in-situ by additive manufacturing

The natural oxide layer on the surface of steel powder particles, together with a residual oxygen content in the process chamber, leads to oxides in the microstructure of many steels processed by L-PBF. Saeidi et al. describe the presence of Cr-rich, amorphous silicates in the

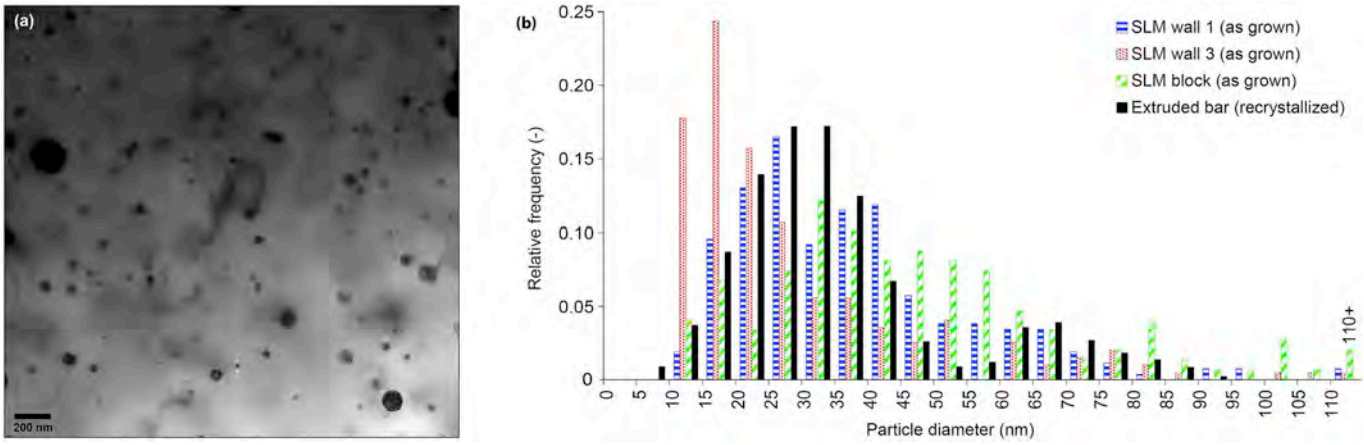

Fig. 27. PM2000 ODS steel produced by L-PBF after mechanical alloying. (a) TEM micrograph showing the oxide dispersion in the ferritic matrix and (b) the corresponding oxide size distribution for SLM (L-PBF) and conventionally produced material. Oxides after L-PBF processing are slightly coarser than in conventionally-produced material, but are homogeneously dispersed. Adapted with permission from Ref. [188].

microstructure of L-PBF-produced 316L austenitic stainless steel [47,193]. Such oxides are probably present in all L-PBF-produced steels, but few authors notice or comment on them. Saeidi et al. ascribe the higher than expected hardness of austenitic stainless steel, compared with conventionally produced one, partly to the existence of these oxides. The room-temperature mechanical properties, in particular the ductility of their samples compares favourably with 304L ODS austenitic stainless steel produced by HIP.

Also other authors notice the presence of oxides in as-L-PBF-produced steels, be it in 316L austenitic stainless steel (mostly Si- and Mn-rich oxides) [27,50,194], Invar alloy (Fe–36Ni, with Fe_3O_4 oxides) [195] or maraging steels (TiO_2) [124], see Fig. 28. As mentioned before, often a bimodal oxide size distribution is found: besides oxides tens of nm in diameter, also coarser oxides, 10–100 μm are found [131,196]. The coarse oxides usually occur when the material is processed with low laser power and, importantly, slow scanning.

These findings led to attempts to synthesize ODS steels not by the laborious and energy- and time-intensive process of mechanically alloying, but by intentional oxidation in-situ during the L-PBF process. Oxygen can be introduced directly into the powder during atomization using an oxidising gas atmosphere [197], or by using an artificially oxygen-enriched process atmosphere in L-PBF [198,199] or in DED [200]. In the latter case, incursion of air in the region above the melt pool also led to the emergence of nitrides next to the expected oxides. In most studies, using an oxidising process atmosphere led to an increase in the number density of oxide particles.

Oxides can also be introduced as nano-particles into the steels without mechanical alloying. Doñate-Buendía et al. use laser-generated Y_2O_3 nano-particles (among others) electrochemically dispersed on micrometre-sized PM2000 matrix powder in the DED process [201]. The thus synthesized ODS steel performed similarly to oxide-free PM2000 matrix powder processed by DED, but showed a 22% increase in compressive yield strength at a temperature of 600 °C.

It is remarkable that the size of the small oxide particles in all these studies is between 10 and 80 nm despite the wildly varying processing routes. This fact suggests that the oxides are actually dissolved in the liquid steel melt during AM processing. A part of the oxygen floats to the melt pool surface and a) is ejected as spatter [202] b) keeps being floated up layer by layer, until it forms the surface "slag layer", or c) forms coarse oxide inside the material, in particular at slow scanning speeds. The remaining oxygen presumably precipitates from the melt, leading to the often-observed small and round oxide particles. It must by noted, however, that there is no experimental proof for this hypothesized mechanism yet, beyond the similarity in particle size.

6.3. Other reinforcing particles

In a similar way as in ODS steels, various authors have processed steels (mostly austenitic stainless steels) with the aim to produce a steel matrix reinforced with nanometre-sized hard particles. This includes processing of TiB_2 nano-powders with steel micro-powder [203,204] and the in-situ formation of TiC particles by the reaction Ti + C→TiC in the melt pool [205,206]. As mentioned in the introduction, a full review of these MMC-type materials is, however, outside the scope of this review.

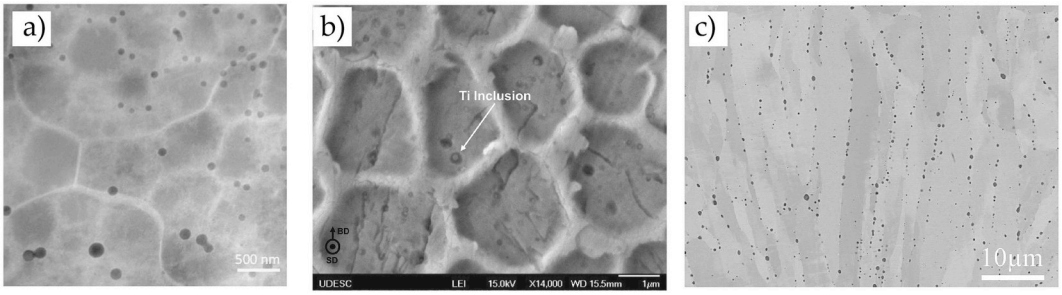

Fig. 28. Three different materials produced by L-PBF including oxide particles with diameters below 1 μm (a) Si-rich oxides in a 316L stainless steel [47], b) TiO_2 inclusions in a 18Ni-300 maraging steel [124], c) oxides in Invar 36 [195]. Adapted from the references with permission.

7. Conclusions

Steels are mankind's most successful, important, affordable and available structural materials. They often serve in the form of enabling, backbone, and safety-critical components in key products in all fields relevant to society such as transportation, energy conversion, safety, health, infrastructure and manufacturing. Examples are large buildings, cars, ships, tools, spaceships, wind turbines, and nuclear power plants.

The published studies about the additive manufacturing of steels reflect the opportunities and challenges of this manufacturing pathway and the wide variety of available steel grades. For some steels classes and specific AM processes, large numbers of studies have been performed. For other steel variants and AM processes, the number of published works is still small and in some cases there is disagreement among the published results regarding microstructure and properties. Generally, we can draw the following conclusions:

- Steels can be processed in fusion AM processes to almost full relative density. A small volume fraction of process-typical defects such as pores remains in the microstructure. Some grades, especially carbon-bearing tool steels, require pre-heating of the substrate plate to achieve crack-free parts.
- The microstructure of AM-produced steels is, as is to be expected, dominated by the solidification and solid-state phase transformations. Its features are smaller than those in the conventionally produced counterparts, usually at least by an order of magnitude.
- For some steels, the phases in the as-produced microstructure differ greatly from the intended in-use microstructure. This is due to the high cooling rates during AM, which may change the primary solidification phase, but also because microsegregation upon solidification leads to chemical inhomogeneity and hence locally differing phase stabilities. Additionally, high cooling rates after solidification can lead to incomplete phase transformations (e.g. austenite formation in duplex stainless steels), while the intrinsic heat treatment, in particular during DED, can trigger precipitation reactions (e.g. in-situ tempering in tool steels).
- Because of the difference between intended and observed microstructures, many AM-produced steels require a post-heat treatment. This may differ from the usually-applied and standardised heat treatment.
- As is typical for microstructures of steels solidified in a strong temperature gradient, steels produced by AM usually show a pronounced crystallographic <001> fibre texture along the build direction. However, solid-state phase transformations upon cooling, in particular the martensite transformation e.g. in tool steels, leads to a weakening of the texture.
- The hardness and tensile strength of AM-produced steels typically matches or even exceeds that of their conventionally-produced counterparts. This is variously attributed to the fine microstructure, to its hierarchical nature, and to precipitates present in the microstructure after processing. The ductility, however, is often found to be inferior. The crucial factor to achieve high elongation at fracture is the complete elimination of fracture initiation sites such as microcracks or lack-of-bonding defects. For some material/process combinations where this is achieved, the ductility has been shown to match conventionally-produced material.
- Similar to ductility, also the fatigue strength depends mostly on surface and internal defects. Samples tested with as-produced surface conditions usually show a poor fatigue life. Post-treatments such as hot isostatic pressing and surface machining considerably improve fatigue properties. In some cases, thus-treated specimens show a comparable fatigue life as conventionally-produced specimens.
- The corrosion properties of AM-produced steels, mainly stainless steels, is typically superior to those of conventionally-produced material. Again, this is often attributed to the fine microstructure, sometimes also to the special texture and the two-phase nature of AM-produced stainless steels. The research into the reasons for the improved corrosion resistance is still in its early stages.

Steels can be well processed by AM and display properties that are in some cases exceeding those of conventionally-produced steels (strength, corrosion resistance), but in other cases lagging behind (ductility, fatigue life). It is important to keep these strengths and weaknesses in mind when designing parts to be manufactured from steel by AM or use these observations for the custom-design of AM-specific steels with better properties considering these potential areas of weakness. Likewise, the AM-typical requirements on modified heat treatments and, potentially, mechanical anisotropy need to be taken into account. For instance, texture related anisotropy in diffusion, magnetic and stiffness features need to be mitigated or can be utilized.

8. Outlook

In the future, additional research is required to overcome the challenges in AM steel processing. In some cases, the underlying reasons for the observed properties need to be clarified, e.g. in the interesting corrosion resistance of L-PBF produced stainless steels. In other cases, the interplay between alloy and processing is needs to be improved either by adapted alloys or by improved processing, e.g. in the case of C-bearing tool steels experiencing a relatively uncontrolled in-situ-tempering during AM processing. Some combinations of alloys and processes are not explored yet, e.g. there are only limited studies of steels in E-PBF.

Some of this research is already ongoing, especially in the area of microstructure modification by process control. At the end of this review, two points merit consideration. First, the vast majority of research being conducted on AM of steels up to now is about the processing of existing alloys with new processes. However, alloys are always developed considering a certain processing route which in turn lends the material a beneficial microstructure and thus property profile. Therefore, almost all steels in AM at the moment are used in a way that was initially not intended. While this works well in some cases (e.g. austenitic stainless steels), other steel classes are more difficult to process (carbon-bearing tool steels). This disadvantage can be ameliorated by substitution (employ maraging steels instead), process modification (develop high-temperature pre-heating systems), but also by alloy modification. This latter possibility is currently mostly being neglected, but might evolve into a promising research field in the near future, with some companies already today marketing steel grades "developed specifically for AM". The aim of such alloy development should not only be to improve the processability of steels in AM, but also to exploit the unique features of AM processes to produce steels with improved properties. An example are the high cooling rates in conjunction with the intrinsic re-heating during sequential layer building enabling an order of magnitude high precipitate number densities compared to conventional manufacturing routes in the case of some maraging steels.

The second point pertains to the definition of "steel". In this review, as well as in the vast majority of published studies, steel refers exclusively to iron-base alloys intended for structural applications. There is, however, increasing interest in utilizing AM for making parts of iron-base alloys with functional properties. This includes the invar features of FeNi or FeCoNi steels which have over a wide temperature range a negligible coefficient of thermal expansion and are therefore products with key relevance for applications in the liquid-gas, precision machinery and space industries. In these fields, AM produced invar alloys are already used for economic reasons and further growth is envisaged. For instance, Invar 36 (Fe-36 wt%Ni) can be well processed by L-PBF [207–209] and by DED [210]. Another example for functional, iron-based alloys are electrical steels. These soft-magnetic materials require a specific crystallographic texture (Goss texture, {011}<100>) to achieve the low hysteresis losses that make them desirable for applications e.g. in transformers and electric motors. In this application

domain, the ability of AM to produce functional parts with complex geometries opens a very promising field of research as advanced design strategies for the ongoing electrification efforts in transportation, construction and manufacturing often require parts with custom-designed shapes. Additionally, if the necessity to deform electrical steel by rolling is removed by AM processing, Fe–Si-alloys with increased Si content may be used, which shows a higher electrical resistivity compared to conventional electrical steel (up to 3.5%Si) and hence a lower hysteresis loss [211–213]. Further iron-based functional materials that are considered for use in AM include amorphous, nanocrystalline, and magnetocaloric materials (see Ref. [214] for a recent review).

Data availability statement

The raw/processed data required to reproduce these findings cannot be shared at this time because this being a review article, it was taken from the published literature.

Acknowledgements

EAJ, AK and PK are grateful to the Strategic Cooperation of the Max-Planck Society and the Fraunhofer Society for funding under the APro-LAM project. PB acknowledges funding by the DFG under grant number JA2482/2-1. AH is grateful to the graduate school SurMat for funding.

References

[1] D. Herzog, V. Seyda, E. Wycisk, C. Emmelmann, Additive manufacturing of metals, Acta Mater. 117 (2016) 371–392, https://doi.org/10.1016/j.actamat.2016.07.019.
[2] V. Manakari, G. Parande, M. Gupta, H.F. Lopez, Selective laser melting of magnesium and magnesium alloy powders, A Review (2017), https://doi.org/10.3390/met7010002.
[3] D. Gu, W. Meiners, K. Wissenbach, R. Poprawe, Laser additive manufacturing of metallic components: materials, processes and mechanisms, Int. Mater. Rev. 57 (2012) 133–164, https://doi.org/10.1179/1743280411Y.0000000014.
[4] S. Gorsse, C. Hutchinson, M. Gouné, R. Banerjee, Additive manufacturing of metals: a brief review of the characteristic microstructures and properties of steels, Ti-6Al-4V and high-entropy alloys, Sci. Technol. Adv. Mater. 18 (2017) 584–610, https://doi.org/10.1080/14686996.2017.1361305.
[5] H. Fayazfar, M. Salarian, A. Rogalsky, D. Sarker, P. Russo, V. Paserin, E. Toyserkani, A critical review of powder-based additive manufacturing of ferrous alloys: process parameters, microstructure and mechanical properties, Mater. Des. 144 (2018) 98–128, https://doi.org/10.1016/j.matdes.2018.02.018.
[6] S. Dadbakhsh, R. Mertens, L. Hao, J. Van Humbeeck, J.-P. Kruth, Selective laser melting to manufacture “in situ” metal matrix composites: a review, Adv. Eng. Mater. 1801244 (2019) 1801244, https://doi.org/10.1002/adem.201801244.
[7] D. Lehmhus, M. Busse, A. von Hehl, E. Jägle, State of the art and emerging trends in additive manufacturing: from multi-material processes to 3D printed electronics, MATEC Web Conf 188 (2018), 03013, https://doi.org/10.1051/matecconf/201818803013.
[8] C.N. Hsiao, C.S. Chiou, J.R. Yang, Aging reactions in a 17-4 PH stainless steel, Mater. Chem. Phys. 74 (2002) 134–142, https://doi.org/10.1016/S0254-0584(01)00460-6.
[9] S.L. Campanelli, N. Contuzzi, A. Angelastro, A.D. Ludovico, Capabilities and performances of the selective laser melting process, in: M.J. Er (Ed.), New Trends Technol. Devices, Comput. Commun, Ind. Syst., Sciyo, 2012, pp. 233–252, https://doi.org/10.5772/10432.
[10] A. Armillotta, R. Baraggi, S. Fasoli, SLM tooling for die casting with conformal cooling channels, Int. J. Adv. Manuf. Technol. 71 (2014) 573–583, https://doi.org/10.1007/s00170-013-5523-7.
[11] M. Mazur, M. Leary, M. McMillan, J. Elambasseril, M. Brandt, SLM additive manufacture of H13 tool steel with conformal cooling and structural lattices, Rapid Prototyp. J. 22 (2016) 504–518, https://doi.org/10.1108/RPJ-06-2014-0075.
[12] M. Mazur, P. Brincat, M. Leary, M. Brandt, Numerical and experimental evaluation of a conformally cooled H13 steel injection mould manufactured with selective laser melting, Int. J. Adv. Manuf. Technol. 93 (2017) 881–900, https://doi.org/10.1007/s00170-017-0426-7.
[13] L.E. Rännar, A. Glad, C.G. Gustafson, Efficient cooling with tool inserts manufactured by electron beam melting, Rapid Prototyp. J. 13 (2007) 128–135, https://doi.org/10.1108/13552540710750870.
[14] S. Kumar, S. Pityana, Laser-based additive manufacturing of metals, Adv. Mater. Res. 227 (2011) 92–95. https://doi.org/10.4028/www.scientific.net/AMR.227.92.
[15] M. Shiomi, F. Abe, M. Matsumoto, K. Uematsu, K. Osakada, The manufacturing of hard tools from metallic powders by selective laser melting, J. Mater. Process. Technol. 111 (2002) 210–213, https://doi.org/10.1016/s0924-0136(01)00522-2.
[16] T.H.C. Childs, C. Hauser, M. Badrossamay, Selective laser sintering (melting) of stainless and tool steel powders: experiments and modelling, Proc. Inst. Mech. Eng. B J. Eng. Manuf. 219 (2005) 339–357, https://doi.org/10.1243/095440505X8109.
[17] T.H.C. Childs, C. Hauser, M. Badrossamay, Mapping and modelling single scan track formation in direct metal selective laser melting, CIRP Ann. - Manuf. Technol. 53 (2004) 191–194, https://doi.org/10.1016/S0007-8506(07)60676-3.
[18] M. Badrossamay, T.H.C. Childs, Further studies in selective laser melting of stainless and tool steel powders, Int. J. Mach. Tool Manuf. 47 (2007) 779–784, https://doi.org/10.1016/j.ijmachtools.2006.09.013.
[19] I. Tolosa, F. Garciandía, F. Zubiri, F. Zapirain, A. Esnaola, Study of mechanical properties of AISI 316 stainless steel processed by “selective laser melting”, following different manufacturing strategies, Int. J. Adv. Manuf. Technol. 51 (2010) 639–647, https://doi.org/10.1007/s00170-010-2631-5.
[20] C.Y. Yap, C.K. Chua, Z.L. Dong, Z.H. Liu, D.Q. Zhang, L.E. Loh, S.L. Sing, Review of selective laser melting: materials and applications, Appl. Phys. Rev. 2 (2015), 041101, https://doi.org/10.1063/1.4935926.
[21] C. Kamath, B. El-dasher, G.F. Gallegos, W.E. King, A. Sisto, Density of additively-manufactured, 316L SS parts using laser powder-bed fusion at powers up to 400 W, Int. J. Adv. Manuf. Technol. 74 (2014) 65–78, https://doi.org/10.1007/s00170-014-5954-9.
[22] M. Thomas, G.J. Baxter, I. Todd, Normalised model-based processing diagrams for additive layer manufacture of engineering alloys, Acta Mater. 108 (2016) 26–35, https://doi.org/10.1016/j.actamat.2016.02.025.
[23] J. Metelkova, Y. Kinds, K. Kempen, C. de Formanoir, A. Witvrouw, B. Van Hooreweder, On the influence of laser defocusing in Selective Laser Melting of 316L, Addit. Manuf. 23 (2018) 161–169, https://doi.org/10.1016/j.addma.2018.08.006.
[24] H. Yu, J. Yang, J. Yin, Z. Wang, X. Zeng, Comparison on mechanical anisotropies of selective laser melted Ti-6Al-4V alloy and 304 stainless steel, Mater. Sci. Eng. A 695 (2017) 92–100, https://doi.org/10.1016/j.msea.2017.04.031.
[25] E. Yasa, J.-P. Kruth, Microstructural investigation of Selective Laser Melting 316L stainless steel parts exposed to laser re-melting, Procedia Eng 19 (2011) 389–395, https://doi.org/10.1016/J.PROENG.2011.11.130.
[26] J. Suryawanshi, K.G. Prashanth, U. Ramamurty, Mechanical behavior of selective laser melted 316L stainless steel, Mater. Sci. Eng. A 696 (2017) 113–121, https://doi.org/10.1016/j.msea.2017.04.058.
[27] Y. Zhong, L. Liu, S. Wikman, D. Cui, Z. Shen, Intragranular cellular segregation network structure strengthening 316L stainless steel prepared by selective laser melting, J. Nucl. Mater. 470 (2016) 170–178, https://doi.org/10.1016/j.jnucmat.2015.12.034.
[28] B. Blinn, M. Klein, C. Gläßner, M. Smaga, J.C. Aurich, T. Beck, B. Blinn, M. Klein, C. Gläßner, M. Smaga, J.C. Aurich, T. Beck, An investigation of the microstructure and fatigue behavior of additively manufactured AISI 316L stainless steel with regard to the influence of heat treatment, Metals 8 (2018) 220, https://doi.org/10.3390/met8040220.
[29] A. Riemer, S. Leuders, M. Thöne, H.A. Richard, T. Tröster, T. Niendorf, On the fatigue crack growth behavior in 316L stainless steel manufactured by selective laser melting, Eng. Fract. Mech. 120 (2014) 15–25, https://doi.org/10.1016/J.ENGFRACMECH.2014.03.008.
[30] J.W. Elmer, S.M. Allen, T.W. Eagar, Microstructural development during solidification of stainless steel alloys, Metall. Trans. A. 20 (1989) 2117–2131, https://doi.org/10.1007/BF02650298.
[31] J. Brooks, M. Baskes, F. Greulich, Solidification modeling and solid-state transformations in high-energy density stainless steel welds, Met. Mater. 22 (1991). http://www.springerlink.com/index/41J7283664306878.pdf. (Accessed 25 March 2013).
[32] A. Yadollahi, N. Shamsaei, S.M. Thompson, D.W. Seely, Effects of process time interval and heat treatment on the mechanical and microstructural properties of direct laser deposited 316L stainless steel, Mater. Sci. Eng. A 644 (2015) 171–183, https://doi.org/10.1016/j.msea.2015.07.056.
[33] M. Ziętala, T. Durejko, M. Polański, I. Kunce, T. Płociński, W. Zieliński, M. Łazińska, W. Stępniowski, T. Czujko, K.J. Kurzydłowski, Z. Bojar, The microstructure, mechanical properties and corrosion resistance of 316L stainless steel fabricated using laser engineered net shaping, Mater. Sci. Eng. A 677 (2016) 1–10, https://doi.org/10.1016/j.msea.2016.09.028.
[34] P.G.E. Jerrard, L. Hao, K.E. Evans, Experimental investigation into selective laser melting of austenitic and martensitic stainless steel powder mixtures, Proc. Inst. Mech. Eng. B J. Eng. Manuf. 223 (2009) 1409–1416, https://doi.org/10.1243/09544054JEM1574.
[35] K. Abd-Elghany, D.L. Bourell, Property evaluation of 304L stainless steel fabricated by selective laser melting, Rapid Prototyp. J. 18 (2012) 420–428, https://doi.org/10.1108/13552541211250418.
[36] T. Niendorf, S. Leuders, A. Riemer, H.A. Richard, T. Tröster, D. Schwarze, Highly anisotropic steel processed by selective laser melting, Metall. Mater. Trans. B 44 (2013) 794–796, https://doi.org/10.1007/s11663-013-9875-z.
[37] J.M. Vitek, A. Dasgupta, S.A. David, Microstructural modification of austenitic stainless steels by rapid solidification, Metall. Trans. A. 14 (1983) 1833–1841, https://doi.org/10.1007/BF02645553.
[38] Y.M. Wang, T. Voisin, J.T. McKeown, J. Ye, N.P. Calta, Z. Li, Z. Zeng, Y. Zhang, W. Chen, T.T. Roehling, R.T. Ott, M.K. Santala, P.J. Depond, M.J. Matthews, A. V. Hamza, T. Zhu, Additively manufactured hierarchical stainless steels with high strength and ductility, Nat. Mater. 17 (2018) 63–70, https://doi.org/10.1038/NMAT5021.

[39] J. Olsén, Z. Shen, L. Liu, A. Koptyug, L.-E. Rännar, Micro- and macro-structural heterogeneities in 316L stainless steel prepared by electron-beam melting, Mater. Char. 141 (2018) 1–7, https://doi.org/10.1016/j.matchar.2018.04.026.
[40] I. Todd, Metallurgy: printing steels, Nat. Mater. 17 (2017) 13–14, https://doi.org/10.1038/nmat5042.
[41] Y. Hong, C. Zhou, Y. Zheng, L. Zhang, J. Zheng, X. Chen, B. An, Formation of strain-induced martensite in selective laser melting austenitic stainless steel, Mater. Sci. Eng. A 740–741 (2019) 420–426, https://doi.org/10.1016/j.msea.2018.10.121.
[42] M. Shamsujjoha, S.R. Agnew, J.M. Fitz-Gerald, W.R. Moore, T.A. Newman, High strength and ductility of additively manufactured 316L stainless steel explained, Metall. Mater. Trans. A 49 (2018) 3011–3027, https://doi.org/10.1007/s11661-018-4607-2.
[43] S.-H. Sun, T. Ishimoto, K. Hagihara, Y. Tsutsumi, T. Hanawa, T. Nakano, Excellent mechanical and corrosion properties of austenitic stainless steel with a unique crystallographic lamellar microstructure via selective laser melting, Scr. Mater. 159 (2019) 89–93, https://doi.org/10.1016/j.scriptamat.2018.09.017.
[44] Z. Sun, X. Tan, S.B. Tor, C.K. Chua, Simultaneously enhanced strength and ductility for 3D-printed stainless steel 316L by selective laser melting, NPG Asia Mater. 10 (2018) 127–136, https://doi.org/10.1038/s41427-018-0018-5.
[45] K. Saeidi, X. Gao, F. Lofaj, L. Kvetková, Z.J. Shen, Transformation of austenite to duplex austenite-ferrite assembly in annealed stainless steel 316L consolidated by laser melting, J. Alloy. Comp. 633 (2015) 463–469, https://doi.org/10.1016/J.JALLCOM.2015.01.249.
[46] Y.J. Yin, J.Q. Sun, J. Guo, X.F. Kan, D.C. Yang, Mechanism of high yield strength and yield ratio of 316 L stainless steel by additive manufacturing, Mater. Sci. Eng. A 744 (2019) 773–777, https://doi.org/10.1016/j.msea.2018.12.092.
[47] K. Saeidi, X. Gao, Y. Zhong, Z.J.J. Shen, Hardened austenite steel with columnar sub-grain structure formed by laser melting, Mater. Sci. Eng. A 625 (2014) 221–229, https://doi.org/10.1016/j.msea.2014.12.018.
[48] K. Guan, Z. Wang, M. Gao, X. Li, X. Zeng, Effects of processing parameters on tensile properties of selective laser melted 304 stainless steel, Mater. Des. 50 (2013) 581–586, https://doi.org/10.1016/J.MATDES.2013.03.056.
[49] J.J. Lewandowski, M. Seifi, Metal additive manufacturing: a review of mechanical properties, Annu. Rev. Mater. Res. 4614 (2016), https://doi.org/10.1146/annurev-matsci-070115-032024.
[50] X. Lou, P.L. Andresen, R.B. Rebak, Oxide inclusions in laser additive manufactured stainless steel and their effects on impact toughness and stress corrosion cracking behavior, J. Nucl. Mater. 499 (2018) 182–190, https://doi.org/10.1016/J.JNUCMAT.2017.11.036.
[51] H.D. Carlton, A. Haboub, G.F. Gallegos, D.Y. Parkinson, A.A. MacDowell, Damage evolution and failure mechanisms in additively manufactured stainless steel, Mater. Sci. Eng. A 651 (2016) 406–414, https://doi.org/10.1016/j.msea.2015.10.073.
[52] Z. Wang, T.A. Palmer, A.M. Beese, Effect of processing parameters on microstructure and tensile properties of austenitic stainless steel 304L made by directed energy deposition additive manufacturing, Acta Mater. 110 (2016) 226–235, https://doi.org/10.1016/j.actamat.2016.03.019.
[53] A.B. Spierings, T.L. Starr, K. Wegener, Fatigue performance of additive manufactured metallic parts, Rapid Prototyp. J. 19 (2013) 88–94, https://doi.org/10.1108/13552541311302932.
[54] J. Suryawanshi, T. Baskaran, O. Prakash, S.B. Arya, U. Ramamurty, On the corrosion resistance of some selective laser melted alloys, Materialia 3 (2018) 153–161, https://doi.org/10.1016/j.mtla.2018.08.022.
[55] G. Sander, S. Thomas, V. Cruz, M. Jurg, N. Birbilis, X. Gao, M. Brameld, C. R. Hutchinson, On the corrosion and metastable pitting characteristics of 316L stainless steel produced by selective laser melting, J. Electrochem. Soc. 164 (2017) C250–C257, https://doi.org/10.1149/2.0551706jes.
[56] M.R. Stoudt, R.E. Ricker, E.A. Lass, L.E. Levine, Influence of postbuild microstructure on the electrochemical behavior of additively manufactured 17-4 PH stainless steel, J. Occup. Med. 69 (2017) 506–515, https://doi.org/10.1007/s11837-016-2237-y.
[57] Q. Chao, V. Cruz, S. Thomas, N. Birbilis, P. Collins, A. Taylor, P.D. Hodgson, D. Fabijanic, On the enhanced corrosion resistance of a selective laser melted austenitic stainless steel, Scr. Mater. 141 (2017) 94–98, https://doi.org/10.1016/J.SCRIPTAMAT.2017.07.037.
[58] E.A. Jägle, Z. Sheng, L. Wu, L. Lu, J. Risse, A. Weisheit, D. Raabe, Precipitation reactions in age-hardenable alloys during laser additive manufacturing, JOM (J. Occup. Med.) 68 (2016) 943–949, https://doi.org/10.1007/s11837-015-1764-2.
[59] X. Lou, M. Song, P.W. Emigh, M.A. Othon, P.L. Andresen, On the stress corrosion crack growth behaviour in high temperature water of 316L stainless steel made by laser powder bed fusion additive manufacturing, Corros. Sci. 128 (2017) 140–153, https://doi.org/10.1016/j.corsci.2017.09.017.
[60] X. Lou, M.A. Othon, R.B. Rebak, Corrosion fatigue crack growth of laser additively-manufactured 316L stainless steel in high temperature water, Corros. Sci. 127 (2017) 120–130, https://doi.org/10.1016/j.corsci.2017.08.023.
[61] C. Haase, J. Bültmann, J. Hof, S. Ziegler, S. Bremen, C. Hinke, A. Schwedt, U. Prahl, W. Bleck, C. Haase, J. Bültmann, J. Hof, S. Ziegler, S. Bremen, C. Hinke, A. Schwedt, U. Prahl, W. Bleck, Exploiting process-related advantages of selective laser melting for the production of high-manganese steel, Materials 10 (2017) 56, https://doi.org/10.3390/ma10010056.
[62] F. Kies, P. Köhnen, M.B. Wilms, F. Brasche, K.G. Pradeep, A. Schwedt, S. Richter, A. Weisheit, J.H. Schleifenbaum, C. Haase, Design of high-manganese steels for additive manufacturing applications with energy-absorption functionality, Mater. Des. 160 (2018) 1250–1264, https://doi.org/10.1016/J.MATDES.2018.10.051.
[63] T. Niendorf, F. Brenne, Steel showing twinning-induced plasticity processed by selective laser melting - an additively manufactured high performance material, Mater. Char. 85 (2013) 57–63, https://doi.org/10.1016/j.matchar.2013.08.010.
[64] T. Niendorf, F. Brenne, P. Hoyer, D. Schwarze, M. Schaper, R. Grothe, M. Wiesener, G. Grundmeier, H.J. Maier, Processing of new materials by additive manufacturing: iron-based alloys containing silver for biomedical applications, Metall. Mater. Trans. A 46 (2015) 2829–2833, https://doi.org/10.1007/s11661-015-2932-2.
[65] J.-O. Nilsson, Super duplex stainless steels, Mater. Sci. Technol. 8 (1992) 685–700, https://doi.org/10.1179/mst.1992.8.8.685.
[66] K. Davidson, S. Singamneni, Selective laser melting of duplex stainless steel powders: an investigation, Mater. Manuf. Process. 31 (2016) 1543–1555, https://doi.org/10.1080/10426914.2015.1090605.
[67] K. Saeidi, L. Kevetkova, F. Lofaj, Z. Shen, Novel ferritic stainless steel formed by laser melting from duplex stainless steel powder with advanced mechanical properties and high ductility, Mater. Sci. Eng. A 665 (2016) 59–65, https://doi.org/10.1016/j.msea.2016.04.027.
[68] K. Saeidi, S. Alvi, F. Lofaj, V.I. Petkov, F. Akhtar, Advanced mechanical strength in post heat treated SLM 2507 at room and high temperature promoted by hard/ductile sigma precipitates, Metals 9 (2019) 199, https://doi.org/10.3390/met9020199.
[69] F. Hengsbach, P. Koppa, K. Duschik, M.J. Holzweissig, M. Burns, J. Nellesen, W. Tillmann, T. Tröster, K.-P. Hoyer, M. Schaper, Duplex stainless steel fabricated by selective laser melting - microstructural and mechanical properties, Mater. Des. 133 (2017) 136–142, https://doi.org/10.1016/j.matdes.2017.07.046.
[70] C. Sørensen, B.M. Brønstad, R. Aune, A. Robertstad, X. Ren, M. Lervåg, M. Eriksson, B. Nyhus, O.M. Akselsen, Additive manufacture of superduplex stainless steel using WAAM, MATEC Web Conf 188 (2018), 03014, https://doi.org/10.1051/matecconf/201818803014.
[71] K.P. Davidson, S. Singamneni, Magnetic characterization of selective laser-melted SAF 2507 duplex stainless steel, J. Occup. Med. 69 (2017) 569–574, https://doi.org/10.1007/s11837-016-2193-6.
[72] J. Hunt, F. Derguti, I. Todd, Selection of steels suitable for additive layer manufacturing, Ironmak. Steelmak. 41 (2014) 254–256, https://doi.org/10.1179/0301923314Z.000000000269.
[73] M. Murayama, K. Hono, Y. Katayama, Microstructural evolution in a 17-4 PH stainless steel after aging at 400 °C, Metall. Mater. Trans. A 30 (1999) 345–353, https://doi.org/10.1007/s11661-999-0323-2.
[74] H. Asgari, M. Mohammadi, Microstructure and mechanical properties of stainless steel CX manufactured by Direct Metal Laser Sintering, Mater. Sci. Eng. A 709 (2018) 82–89, https://doi.org/10.1016/j.msea.2017.10.045.
[75] M. Mahmoudi, A. Elwany, A. Yadollahi, S.M. Thompson, L. Bian, N. Shamsaei, Mechanical properties and microstructural characterization of selective laser melted 17-4 PH stainless steel, Rapid Prototyp. J. 23 (2017) 280–294, https://doi.org/10.1108/RPJ-12-2015-0192.
[76] A.A. Adeyemi, E. Akinlabi, R.M. Mahamood, K.O. Sanusi, S. Pityana, M. Tlotleng, Influence of laser power on microstructure of laser metal deposited 17-4 ph stainless steel, IOP Conf. Ser. Mater. Sci. Eng. 225 (2017), 012028, https://doi.org/10.1088/1757-899X/225/1/012028.
[77] R. Rashid, S.H. Masood, D. Ruan, S. Palanisamy, R.A. Rahman Rashid, M. Brandt, Effect of scan strategy on density and metallurgical properties of 17-4PH parts printed by Selective Laser Melting (SLM), J. Mater. Process. Technol. 249 (2017) 502–511, https://doi.org/10.1016/J.JMATPROTEC.2017.06.023.
[78] Z. Hu, H. Zhu, H. Zhang, X. Zeng, Experimental investigation on selective laser melting of 17-4PH stainless steel, Opt. Laser. Technol. 87 (2017) 17–25, https://doi.org/10.1016/J.OPTLASTEC.2016.07.012.
[79] S. Pasebani, M. Ghayoor, S. Badwe, H. Irrinki, S.V. Atre, Effects of atomizing media and post processing on mechanical properties of 17-4 PH stainless steel manufactured via selective laser melting, Addit. Manuf. 22 (2018) 127–137, https://doi.org/10.1016/J.ADDMA.2018.05.011.
[80] S.D. Meredith, J.S. Zuback, J.S. Keist, T.A. Palmer, Impact of composition on the heat treatment response of additively manufactured 17–4 PH grade stainless steel, Mater. Sci. Eng. A 738 (2018) 44–56, https://doi.org/10.1016/J.MSEA.2018.09.066.
[81] B.C. Salzbrenner, J.M. Rodelas, J.D. Madison, B.H. Jared, L.P. Swiler, Y.L. Shen, B.L. Boyce, High-throughput stochastic tensile performance of additively manufactured stainless steel, J. Mater. Process. Technol. 241 (2017) 1–12, https://doi.org/10.1016/j.jmatprotec.2016.10.023.
[82] L. Facchini, N. Vicente, I. Lonardelli, E. Magalini, P. Robotti, A. Molinari, Metastable Austenite in 17-4 precipitation-hardening stainless steel produced by selective laser melting, Adv. Eng. Mater. 12 (2010) 184–188, https://doi.org/10.1002/adem.200900259.
[83] S. Cheruvathur, E.A. Lass, C.E. Campbell, Additive manufacturing of 17-4 PH stainless steel: post-processing heat treatment to achieve uniform reproducible microstructure, JOM (J. Occup. Med.) 68 (2016) 930–942, https://doi.org/10.1007/s11837-015-1754-4.
[84] B. Clausen, D.W. Brown, J.S. Carpenter, K.D. Clarke, A.J. Clarke, S.C. Vogel, J. D. Bernardin, D. Spernjak, J.M. Thompson, Deformation behavior of additively manufactured GP1 stainless steel, Mater. Sci. Eng. A (2017), https://doi.org/10.1016/j.msea.2017.04.081.
[85] Y. Sun, R.J. Hebert, M. Aindow, Effect of heat treatments on microstructural evolution of additively manufactured and wrought 17-4PH stainless steel, Mater. Des. 156 (2018) 429–440, https://doi.org/10.1016/J.MATDES.2018.07.015.
[86] A. Caballero, J. Ding, S. Ganguly, S. Williams, Wire + Arc Additive Manufacture of 17-4 PH stainless steel: effect of different processing conditions on

microstructure, hardness, and tensile strength, J. Mater. Process. Technol. 268 (2019) 54–62, https://doi.org/10.1016/j.jmatprotec.2019.01.007.
[87] H.K. Rafi, D. Pal, N. Patil, T.L. Starr, B.E. Stucker, Microstructure and mechanical behavior of 17-4 precipitation hardenable steel processed by selective laser melting, J. Mater. Eng. Perform. 23 (2014) 4421–4428, https://doi.org/10.1007/s11665-014-1226-y.
[88] A. Yadollahi, S.M. Thompson, A. Elwany, L. Bian, Effects of building orientation and heat treatment on fatigue behavior of selective laser melted 17-4 PH stainless steel, Int. J. Fatigue 94 (2017) 218–235, https://doi.org/10.1016/J.IJFATIGUE.2016.03.014.
[89] L.E. Murr, E. Martinez, S.M. Gaytan, D.a. Ramirez, B.I. MacHado, P.W. Shindo, J. L. Martinez, F. Medina, J. Wooten, D. Ciscel, U. Ackelid, R.B. Wicker, Microstructural architecture, microstructures, and mechanical properties for a nickel-base superalloy fabricated by electron beam melting, Metall. Mater. Trans. A Phys. Metall. Mater. Sci. 42 (2011) 3491–3508, https://doi.org/10.1007/s11661-011-0748-2.
[90] H. Irrinki, T. Harper, S. Badwe, J. Stitzel, O. Gulsoy, G. Gupta, S.V. Atre, Effects of powder characteristics and processing conditions on the corrosion performance of 17-4 PH stainless steel fabricated by laser-powder bed fusion, Prog. Addit. Manuf. 3 (2018) 39–49, https://doi.org/10.1007/s40964-018-0048-0.
[91] L.E. Murr, E. Martinez, J. Hernandez, S. Collins, K.N. Amato, S.M. Gaytan, P. W. Shindo, Microstructures and properties of 17-4 PH stainless steel fabricated by selective laser melting, J. Mater. Res. Technol. 1 (2012) 167–177, https://doi.org/10.1016/S2238-7854(12)70029-7.
[92] L.E. Murr, E. Martinez, J. Hernandez, S. Collins, K.N. Amato, S.M. Gaytan, P. W. Shindo, Microstructures and properties of 17-4 PH stainless steel fabricated by selective laser melting, J. Mater. Res. Technol. 1 (2012) 167–177, https://doi.org/10.1016/S2238-7854(12)70029-7.
[93] A. Kudzal, B. McWilliams, C. Hofmeister, F. Kellogg, J. Yu, J. Taggart-Scarff, J. Liang, Effect of scan pattern on the microstructure and mechanical properties of Powder Bed Fusion additive manufactured 17-4 stainless steel, Mater. Des. 133 (2017) 205–215, https://doi.org/10.1016/J.MATDES.2017.07.047.
[94] E.A. Lass, M.R. Stoudt, M.E. Williams, Additively manufactured nitrogen-atomized 17-4 PH stainless steel with mechanical properties comparable to wrought, Metall. Mater. Trans. A 50A (2019) 1619–1624, https://doi.org/10.1007/s11661-019-05124-0.
[95] S. Cheruvathur, E.A. Lass, C.E. Campbell, Additive manufacturing of 17-4 PH stainless steel: post-processing heat treatment to achieve uniform reproducible microstructure, JOM (J. Occup. Med.) 68 (2015) 930–942, https://doi.org/10.1007/s11837-015-1754-4.
[96] Z. Guo, J.T. Kindt, Partitioning of size-mismatched impurities to grain boundaries in 2d solid hard-sphere monolayers, Langmuir 34 (2018) 12947–12956, https://doi.org/10.1021/acs.langmuir.8b02633.
[97] T. LeBrun, T. Nakamoto, K. Horikawa, H. Kobayashi, Effect of retained austenite on subsequent thermal processing and resultant mechanical properties of selective laser melted 17-4 PH stainless steel, Mater. Des. 81 (2015) 44–53, https://doi.org/10.1016/j.matdes.2015.05.026.
[98] L. Carneiro, B. Jalalahmadi, A. Ashtekar, Y. Jiang, Cyclic deformation and fatigue behavior of additively manufactured 17–4 PH stainless steel, Int. J. Fatigue 123 (2019) 22–30, https://doi.org/10.1016/J.IJFATIGUE.2019.02.006.
[99] P.D. Nezhadfar, R. Shrestha, N. Phan, N. Shamsaei, Fatigue behavior of additively manufactured 17-4 PH stainless steel: synergistic effects of surface roughness and heat treatment, Int. J. Fatigue 124 (2019) 188–204, https://doi.org/10.1016/J.IJFATIGUE.2019.02.039.
[100] P.D. Nezhadfar, E. Burford, K. Anderson-Wedge, B. Zhang, S. Shao, S. R. Daniewicz, N. Shamsaei, Fatigue crack growth behavior of additively manufactured 17-4 PH stainless steel: effects of build orientation and microstructure, Int. J. Fatigue (2019), https://doi.org/10.1016/J.IJFATIGUE.2019.02.015.
[101] H. Irrinki, J.S.D. Jangam, S. Pasebani, S. Badwe, J. Stitzel, K. Kate, O. Gulsoy, S. V. Atre, Effects of particle characteristics on the microstructure and mechanical properties of 17-4 PH stainless steel fabricated by laser-powder bed fusion, Powder Technol. 331 (2018) 192–203, https://doi.org/10.1016/J.POWTEC.2018.03.025.
[102] M.R. Stoudt, R.E. Ricker, E.A. Lass, L.E. Levine, Influence of postbuild microstructure on the electrochemical behavior of additively manufactured 17-4 PH stainless steel, J. Occup. Med. 69 (2017) 506–515, https://doi.org/10.1007/s11837-016-2237-y.
[103] A. Bayode, S. Pityana, E.T. Akinlabi, M.B. Shongwe, Effect of scanning speed on laser deposited 17-4PH stainless steel, in: 8th Int. Conf. Mech. Intell. Manuf. Technol vol. 2017, IEEE, 2017, pp. 1–5, https://doi.org/10.1109/ICMIMT.2017.7917404.
[104] I. Mathoho, E.T. Akinlabi, N. Arthur, M. Tlotleng, B. Masina, Metallurgical Characteristics of Laser Peened 17-4 PH SS Processed by LENS Technique, 2019, pp. 279–285, https://doi.org/10.1007/978-3-030-05861-6_25.
[105] S. Pal, H.R. Tiyyagura, I. Drstvenšek, C.S. Kumar, The effect of post-processing and machining process parameters on properties of stainless steel PH1 product produced by direct metal laser sintering, Procedia Eng 149 (2016) 359–365, https://doi.org/10.1016/J.PROENG.2016.06.679.
[106] E. Lum, A.N. Palazotto, A. Dempsey, Analysis of the effects of additive manufacturing on the material properties of 15-5PH stainless steel, in: 58th AIAA/ASCE/AHS/ASC Struct. Struct. Dyn. Mater. Conf., American Institute of Aeronautics and Astronautics, Reston, Virginia, 2017, https://doi.org/10.2514/6.2017-1142.
[107] J.D. López-Castro, A. Marchal, L. González, J. Botana, Topological optimization and manufacturing by Direct Metal Laser Sintering of an aeronautical part in 15-5PH stainless steel, Procedia Manuf 13 (2017) 818–824, https://doi.org/10.1016/J.PROMFG.2017.09.121.
[108] H.K. Rafi, T.L. Starr, B.E. Stucker, A comparison of the tensile, fatigue, and fracture behavior of Ti–6Al–4V and 15-5 PH stainless steel parts made by selective laser melting, Int. J. Adv. Manuf. Technol. 69 (2013) 1299–1309, https://doi.org/10.1007/s00170-013-5106-7.
[109] A. Alafaghani, A. Qattawi, M.A.G. Castañón, Effect of manufacturing parameters on the microstructure and mechanical properties of metal laser sintering parts of precipitate hardenable metals, Int. J. Adv. Manuf. Technol. 99 (2018) 2491–2507, https://doi.org/10.1007/s00170-018-2586-5.
[110] D. Roberts, Y. Zhang, I. Charit, J. Zhang, A comparative study of microstructure and high-temperature mechanical properties of 15-5 PH stainless steel processed via additive manufacturing and traditional manufacturing, Prog. Addit. Manuf. 3 (2018) 183–190, https://doi.org/10.1007/s40964-018-0051-5.
[111] M.K. Alam, J. Urbanic, S.M. Saqib, A. Edrisy, Effect of process parameters on the microstructural evolutions of laser cladded 420 martensitic stainless steel, Mater. Sci. Technol. Conf. Proc. (MS&T15), Oct. 4–8 (2015) 35–54.
[112] M.K. Alam, A. Edrisy, J. Urbanic, J. Pineault, Microhardness and stress analysis of laser-cladded AISI 420 martensitic stainless steel, J. Mater. Eng. Perform. 26 (2017) 1076–1084, https://doi.org/10.1007/s11665-017-2541-x.
[113] X. Zhao, Q. Wei, B. Song, Y. Liu, X. Luo, S. Wen, Y. Shi, Fabrication and characterization of AISI 420 stainless steel using selective laser melting, Mater. Manuf. Process. 30 (2015) 1283–1289, https://doi.org/10.1080/10426914.2015.1026351.
[114] C. Tan, K. Zhou, M. Kuang, W. Ma, T. Kuang, Microstructural characterization and properties of selective laser melted maraging steel with different build directions, Sci. Technol. Adv. Mater. 19 (2018) 746–758, https://doi.org/10.1080/14686996.2018.1527645.
[115] W. Sha, Z. Guo, Maraging Steels: Modelling of Microstructure, Properties and Applications, Elsevier, 2009.
[116] K. Kempen, B. Vrancken, S. Buls, L. Thijs, J. Van Humbeeck, J.-P. Kruth, Selective laser melting of crack-free high density M2 high speed steel parts by baseplate preheating, J. Manuf. Sci. Eng. 136 (2014), 061026, https://doi.org/10.1115/1.4028513.
[117] D. Croccolo, M. De Agostinis, S. Fini, G. Olmi, A. Vranic, S. Ciric-Kostic, Influence of the build orientation on the fatigue strength of EOS maraging steel produced by additive metal machine, Fatigue Fract. Eng. Mater. Struct. 39 (2016) 637–647, https://doi.org/10.1111/ffe.12395.
[118] D. Bourell, J.P. Kruth, M. Leu, G. Levy, D. Rosen, A.M. Beese, A. Clare, Materials for additive manufacturing, CIRP Ann. - Manuf. Technol. 66 (2017) 659–681, https://doi.org/10.1016/j.cirp.2017.05.009.
[119] Y. Bai, Y. Yang, D. Wang, M. Zhang, Influence mechanism of parameters process and mechanical properties evolution mechanism of maraging steel 300 by selective laser melting, Mater. Sci. Eng. A 703 (2017) 116–123, https://doi.org/10.1016/j.msea.2017.06.033.
[120] C. Tan, K. Zhou, W. Ma, P. Zhang, M. Liu, T. Kuang, Microstructural evolution, nanoprecipitation behavior and mechanical properties of selective laser melted high-performance grade 300 maraging steel, Mater. Des. 134 (2017) 23–34, https://doi.org/10.1016/j.matdes.2017.08.026.
[121] T. Burkert, A. Fischer, The effects of heat balance on the void formation within marage 300 processed by selective laser melting, solid free, Fabr. Symp. XXXIII (2015) 81–87, https://doi.org/10.1007/s13398-014-0173-7.2.
[122] E.A. Jägle, P. Choi, J. Van Humbeeck, D. Raabe, Precipitation and austenite reversion behavior of a maraging steel produced by selective laser melting, J. Mater. Res. 29 (2014), https://doi.org/10.1557/jmr.2014.204.
[123] T. Becker, D. Dimitrov, The achievable mechanical properties of SLM produced Maraging Steel 300 components, Rapid Prototyp. J. 22 (2016) 487–494, https://doi.org/10.1108/RPJ-08-2014-0096.
[124] S. Bodziak, K.S. Al-Rubaie, L.D. Valentina, F.H. Lafratta, E.C. Santos, A. M. Zanatta, Y. Chen, Precipitation in 300 grade maraging steel built by selective laser melting: aging at 510 °C for 2 h, Mater. Char. (2019) 73–83, https://doi.org/10.1016/j.matchar.2019.02.033.
[125] R. Casati, J. Lemke, M. Vedani, Microstructural and mechanical properties of as built, solution treated and aged 18 Ni (300 grade) maraging steel produced by selective laser melting, Metall. Ital. 109 (2017) 11–20.
[126] G. Casalino, S.L. Campanelli, N. Contuzzi, A.D. Ludovico, Experimental investigation and statistical optimisation of the selective laser melting process of a maraging steel, Opt. Laser. Technol. 65 (2015) 151–158, https://doi.org/10.1016/j.optlastec.2014.07.021.
[127] C. Casavola, S.L. Campanelli, C. Pappalettere, Preliminary investigation on distribution of residual stress generated by the selective laser melting process, J. Strain Anal. Eng. Des. 44 (2009) 93–104, https://doi.org/10.1243/03093247JSA464.
[128] S.L. Campanelli, A. Angelastro, C.G. Signorile, G. Casalino, Investigation on Direct Laser Powder Deposition of 18 Ni (300) Marage Steel Using Mathematical Model and Experimental Characterisation, 2017, pp. 885–895, https://doi.org/10.1007/s00170-016-9135-x.
[129] R. Casati, J. Lemke, A. Tuissi, M. Vedani, Aging behaviour and mechanical performance of 18-Ni 300 steel processed by selective laser melting, Metals 6 (2016) 218, https://doi.org/10.3390/met6090218.
[130] E.A. Jägle, Z. Sheng, P. Kürnsteiner, S. Oclok, A. Weisheit, D. Raabe, Comparison of maraging steel micro- and nanostructure produced conventionally and by Laser Additive Manufacturing, Materials 10 (2017), https://doi.org/10.3390/ma10010008.

[131] K. Kempen, E. Yasa, L. Thijs, J.-P. Kruth, J. Van Humbeeck, Microstructure and mechanical properties of selective laser melted 18Ni-300 steel, Phys. Procedia. 12 (2011) 255–263, https://doi.org/10.1016/j.phpro.2011.03.033.
[132] C. Tan, K. Zhou, X. Tong, Y. Huang, J. Li, W. Ma, F. Li, T. Kuang, Microstructure and mechanical properties of 18Ni-300 Maraging steel fabricated by selective laser melting, 6th Int. Conf. Adv. Des. Manuf. Eng. Microstruct. (2016) 863–870, https://doi.org/10.1002/9781118356074.ch108.
[133] B. Mooney, K.I. Kourousis, R. Raghavendra, Plastic anisotropy of additively manufactured maraging steel: influence of the build orientation and heat treatments, Addit. Manuf. 25 (2019) 19–31, https://doi.org/10.1016/j.addma.2018.10.032.
[134] M.A. Kottman, Additive Manufacturing of Marging 250 Steels for the Rejuvenation and Repurposing of Die Casting Tolling, 2015.
[135] M. Cabeza, G. Castro, P. Merino, G. Pena, M. Román, Laser surface melting: a suitable technique to repair damaged surfaces made in 14 Ni (200 grade) maraging steel, Surf. Coat. Technol. 212 (2012) 159–168, https://doi.org/10.1016/j.surfcoat.2012.09.039.
[136] P. Stoll, A. Spierings, K. Wegener, S. Polster, M. Gebauer, SLM processing of 14 Ni (200 Grade) maraging steel, in: DDMC 2016 Proc. 3rd Fraunhofer Direct Digit. Manuf. Conf., 2016, https://doi.org/10.3929/ethz-a-010802372.
[137] P. Kürnsteiner, M.B. Wilms, A. Weisheit, P. Barriobero-Vila, E.A. Jägle, D. Raabe, Massive nanoprecipitation in an Fe-19Ni-xAl maraging steel triggered by the intrinsic heat treatment during laser metal deposition, Acta Mater. 129 (2017) 52–60, https://doi.org/10.1016/j.actamat.2017.02.069.
[138] W. Sha, Z. Guo, Maraging Steels: Modelling of Microstructure, Properties and Applications, CRC Press, New York, 2009, https://doi.org/10.1533/9781845696931.142.
[139] N. Takata, R. Nishida, A. Suzuki, M. Kobashi, M. Kato, Crystallographic features of microstructure in maraging steel fabricated by selective laser melting, Metals 8 (2018) 440, https://doi.org/10.3390/met8060440.
[140] R. Tewari, S. Mazumder, I.S. Batra, G.K. Dey, S. Banerjee, Precipitation in 18 wt% Ni maraging steel of grade 350, Acta Mater. 48 (2000) 1187–1200, https://doi.org/10.1016/S1359-6454(99)00370-5.
[141] W. Sha, A. Cerezo, G. Smith, Phase chemistry and precipitation reactions in maraging steels: Part IV. Discussion and conclusions, Metall. Trans. A. 24 (1993) 1251–1256. http://link.springer.com/article/10.1007/BF02668193. (Accessed 14 January 2014).
[142] G.Q. Yin, X. Kang, G.P. Zhao, Fatigue properties of the ultra-high strength steel TM210A, Materials 10 (2017), https://doi.org/10.3390/ma10091057.
[143] Q. Chen, T. Nagano, Y. Nakamura, Y. Maeda, N. Kawagoishi, Initiation and propagation behavior of a fatigue crack of maraging steel in high humidity, in: 13th Int. Conf. Fract., 2013.
[144] Z. Liu, C. Chua, K. Leong, K. Kempen, L. Thijs, E. Yasa, J. Van-Humbeeck, J. Kruth, A preliminary investigation on Selective Laser Melting of M2 high speed steel, Innov. Dev. Virtual Phys. Prototyp. 1 (2012) 339–346, https://doi.org/10.1201/b11341-54.
[145] A. Simchi, Direct laser sintering of metal powders: mechanism, kinetics and microstructural features, Mater. Sci. Eng. A 428 (2006) 148–158, https://doi.org/10.1016/j.msea.2006.04.117.
[146] L. Zumofen, C. Beck, A. Kirchheim, H.-J. Denning, Quality related effects of the preheating temperature on laser melted high carbon content steel, Ind. Addit. Manuf. - Proc. Addit. Manuf. Prod. Appl. - AMPA2017 (2017) 210–219, https://doi.org/10.1007/978-3-319-66866-6_21.
[147] K. Kempen, L. Thijs, B. Vrancken, S. Buls, J. Van-Humbeeck, J.-P. Kruth, Lowering thermal gradients in selective laser melting by pre-heating the baseplate, in: Proc. Solid Free, Fabr. Symp., 2013.
[148] C.S. Wright, M. Youseffi, S.P. Akhtar, T.H.C. Childs, C. Hauser, P. Fox, Selective laser melting of prealloyed high alloy steel powder beds, Mater. Sci. Forum 514–516 (2006) 516–523. https://doi.org/10.4028/www.scientific.net/MSF.514-516.516.
[149] Z.H. Liu, D.Q. Zhang, C.K. Chua, K.F. Leong, Crystal structure analysis of M2 high speed steel parts produced by selective laser melting, Mater. Char. 84 (2013) 72–80, https://doi.org/10.1016/j.matchar.2013.07.010.
[150] J. Saewe, C. Gayer, L. Jauer, J. Kunz, C. Broeckmann, J.H. Schleifenbaum, Feasibility investigation for laser powder bed fusion of high-speed steels, Euro PM2018 - Spec. Mater. I (2018).
[151] J. Boes, A. Röttger, C. Mutke, C. Escher, W. Theisen, Microstructure and mechanical properties of X65MoCrWV3-2 cold-work tool steel produced by selective laser melting, Addit. Manuf. 23 (2018) 170–180, https://doi.org/10.1016/j.addma.2018.08.005.
[152] M. Sigl, Ein Beitrag zur Entwicklung des Elektronenstrahlinterns, Technische Universität München, 2008.
[153] R. Casati, M. Coduri, N. Lecis, C. Andrianopoli, M. Vedani, Microstructure and mechanical behavior of hot-work tool steels processed by Selective Laser Melting, Mater. Char. 137 (2018) 50–57, https://doi.org/10.1016/j.matchar.2018.01.015.
[154] C. Scheitler, F. Huber, M. Schmidt, L. Siegel, O. Hentschel, D. Junker, A. Gorunow, Processing of AISI H11 tool steel powder modified with carbon black nanoparticles for the additive manufacturing of forging tools with tailored mechanical properties by means of laser metal deposition (LMD), Metals 8 (2018) 659, https://doi.org/10.3390/met8090659.
[155] D. Junker, O. Hentschel, M. Schmidt, M. Merklein, Investigation of heat treatment strategies for additively-manufactured tools of X37CrMoV5-1, Metals 8 (2018) 854, https://doi.org/10.3390/met8100854.
[156] Y. Ali, S. Barnikol-Oettler, J. Reimann, J. Hildebrand, P. Henckell, J.P. Bergmann, Wire arc additive manufacturing of hot work tool steel with CMT process, J. Mater. Process. Technol. 269 (2019) 109–116, https://doi.org/10.1016/j.jmatprotec.2019.01.034.
[157] F. Huber, C. Bischof, O. Hentschel, J. Heberle, J. Zettl, K.Y. Nagulin, M. Schmidt, Laser beam melting and heat-treatment of 1.2343 (AISI H11) tool steel – microstructure and mechanical properties, Mater. Sci. Eng. A 742 (2019) 109–115, https://doi.org/10.1016/j.msea.2018.11.001.
[158] M.J. Holzweissig, A. Taube, F. Brenne, M. Schaper, T. Niendorf, Microstructural characterization and mechanical performance of hot work tool steel processed by selective laser melting, Metall. Mater. Trans. B Process Metall. Mater. Process. Sci. 46 (2015) 545–549, https://doi.org/10.1007/s11663-014-0267-9.
[159] T.H.C. Childs, C. Hauser, Raster scan selective laser melting of the surface layer of a tool steel powder bed, Proc. Inst. Mech. Eng. B J. Eng. Manuf. 219 (2005) 379–384, https://doi.org/10.1243/095440505X32201.
[160] A.J. Pinkerton, L. Li, Direct additive laser manufacturing using gas- and water-atomised H13 tool steel powders, Int. J. Adv. Manuf. Technol. 25 (2005) 471–479, https://doi.org/10.1007/s00170-003-1844-2.
[161] R. Mertens, B. Vrancken, N. Holmstock, Y. Kinds, J.P. Kruth, J. Van Humbeeck, Influence of powder bed preheating on microstructure and mechanical properties of H13 tool steel SLM parts, Phys. Procedia. 83 (2016) 882–890, https://doi.org/10.1016/j.phpro.2016.08.092.
[162] B. Ren, D. Lu, R. Zhou, Z. Li, J. Guan, Preparation and mechanical properties of selective laser melted H13 steel, J. Mater. Res. (2019) 1–11, https://doi.org/10.1557/jmr.2019.10.
[163] J. Šafka, M. Ackermann, L. Voleský, Structural properties of H13 tool steel parts produced with use of selective laser melting technology, J. Phys. Conf. Ser. 709 (2016), https://doi.org/10.1088/1742-6596/709/1/012004.
[164] J. Mazumder, A. Schifferer, J. Choi, Direct materials deposition: designed macro and microstructure, Mater. Res. Innov. 3 (1999) 118–131, https://doi.org/10.1007/s100190050137.
[165] J.S. Park, J.H. Park, M.G. Lee, J.H. Sung, K.J. Cha, D.H. Kim, Effect of energy input on the characteristic of AISI H13 and D2 tool steels deposited by a directed energy deposition process, Metall. Mater. Trans. A Phys. Metall. Mater. Sci. 47 (2016) 2529–2535, https://doi.org/10.1007/s11661-016-3427-5.
[166] D.L. Zheng, M. Qian, J.J. Yan, J.F. Sun, M. Yan, H.X. Li, X. Jia, Y.L. Li, Selective laser melting of H13: microstructure and residual stress, J. Mater. Sci. 52 (2017) 12476–12485, https://doi.org/10.1007/s10853-017-1380-3.
[167] A. Bohlen, H. Freiße, M. Hunkel, F. Vollertsen, Additive manufacturing of tool steel by laser metal deposition, Procedia CIRP 74 (2018) 192–195, https://doi.org/10.1016/j.procir.2018.08.092.
[168] N.S. Bailey, C. Katinas, Y.C. Shin, Laser direct deposition of AISI H13 tool steel powder with numerical modeling of solid phase transformation, hardness, and residual stresses, J. Mater. Process. Technol. 247 (2017) 223–233, https://doi.org/10.1016/j.jmatprotec.2017.04.020.
[169] L. Xue, J. Chen, S.H. Wang, Freeform laser consolidated H13 and CPM 9V tool steels, Metallogr. Microstruct. Anal. 2 (2013) 67–78, https://doi.org/10.1007/s13632-013-0061-0.
[170] R. Dörfert, J. Zhang, B. Clausen, H. Freiße, J. Schumacher, F. Vollertsen, Comparison of the fatigue strength between additively and conventionally fabricated tool steel 1.2344, Addit. Manuf. 27 (2019) 217–223, https://doi.org/10.1016/j.addma.2019.01.010.
[171] M. Åsberg, G. Fredriksson, S. Hatami, W. Fredriksson, P. Krakhmalev, Influence of post treatment on microstructure, porosity and mechanical properties of additive manufactured H13 tool steel, Mater. Sci. Eng. A 742 (2019) 584–589, https://doi.org/10.1016/j.msea.2018.08.046.
[172] F. Deirmina, N. Peghini, B. Almangour, D. Grzesiak, M. Pellizzari, Heat treatment and properties of a hot work tool steel fabricated by additive manufacturing, Mater. Sci. Eng. A 753 (2019) 109–121, https://doi.org/10.1016/j.msea.2019.03.027.
[173] J. Mazumder, J. Choi, K. Nagarathnam, The direct metal deposition of H13 tool steel for 3-D components, J. Occup. Med. (1997) 55–60. http://www.springerlink.com/index/6018462763247J00.pdf. (Accessed 29 April 2013).
[174] J. Krell, A. Röttger, K. Geenen, W. Theisen, General investigations on processing tool steel X40CrMoV5-1 with selective laser melting, J. Mater. Process. Technol. 255 (2018) 679–688, https://doi.org/10.1016/j.jmatprotec.2018.01.012.
[175] J. Choi, Y. Chang, Characteristics of laser aided direct metal/material deposition process for tool steel, Int. J. Mach. Tool Manuf. 45 (2005) 597–607, https://doi.org/10.1016/j.ijmachtools.2004.08.014.
[176] J. Choi, Y. Hua, Dimensional and material characteristics of direct deposited H13 tool steel by CO2 laser, J. Laser Appl. 16 (2006) 245–251, https://doi.org/10.2351/1.1809638.
[177] J. Brooks, C. Robino, T. Headley, S. Goods, M. Griffith, Microstructure and property optimization of LENS deposited H13 tool steel, in: Proc. 10th Symp. 'Solid Free. Fabr. Austin, Univ. Texas Austin, TX, USA, 1999, pp. 375–382, https://doi.org/10.1016/j.optlastec.2013.04.024. August 1999.
[178] W. Hofmeister, M. Griffith, M. Ensz, J. Smugeresky, Solidification in direct metal deposition by LENS processing, J. Occup. Med. (2001) 30–34.
[179] R. Cottam, J. Wang, V. Luzin, Characterization of microstructure and residual stress in a 3D H13 tool steel component produced by additive manufacturing, J. Mater. Res. 29 (2014) 1978–1986, https://doi.org/10.1557/jmr.2014.190.
[180] D. Cormier, O. Harrysson, H. West, Characterization of H13 steel produced via electron beam melting, Rapid Prototyp. J. 10 (2004) 35–41, https://doi.org/10.1108/13552540410512516.
[181] S.H. Riza, S.H. Masood, C. Wen, Wear behaviour of DMD-generated high-strength steels using multi-factor experiment design on a pin-on-disc apparatus, Int. J. Adv. Manuf. Technol. 87 (2016) 461–477, https://doi.org/10.1007/s00170-016-8505-8.

[182] S.H. Oliari, A.S.C.M. D'Oliveira, M. Schulz, Additive manufacturing of H11 with wire-based laser metal deposition, Soldag. Inspeção. 22 (2017) 466–479, https://doi.org/10.1590/0104-9224/si2204.06.
[183] T.H.C. Childs, C. Hauser, M. Badrossamay, Mapping and modelling single scan track formation in direct metal selective laser melting, CIRP Ann. - Manuf. Technol. 53 (2004) 191–194, https://doi.org/10.1016/S0007-8506(07)60676-3.
[184] H.J. Niu, I.T. Chang, Selective laser sintering of gas and water atomized high speed steel powders, Scr. Mater. 41 (2002) 25–30, https://doi.org/10.1016/s1359-6462(99)00089-5.
[185] M.a. Taha, a.F. Yousef, K.a. Gany, H.a. Sabour, On selective laser melting of ultra high carbon steel: effect of scan speed and post heat treatment, Mater. Werkst. 43 (2012) 913–923, https://doi.org/10.1002/mawe.201200030.
[186] H. Niu, I.T. Chang, Selective laser sintering of gas atomized M2 high speed steel powder, J. Mater. Sci. 35 (2000) 31–38, https://doi.org/10.1023/A:1004720011671.
[187] J.C. Walker, K.M. Berggreen, A.R. Jones, C.J. Sutcliffe, Fabrication of Fe-Cr-Al oxide dispersion strengthened PM2000 alloy using selective laser melting, Adv. Eng. Mater. 11 (2009) 541–546, https://doi.org/10.1002/adem.200800407.
[188] T. Boegelein, S.N. Dryepondt, A. Pandey, K. Dawson, G.J. Tatlock, Mechanical response and deformation mechanisms of ferritic oxide dispersion strengthened steel structures produced by selective laser melting, Acta Mater. 87 (2015) 201–215, https://doi.org/10.1016/j.actamat.2014.12.047.
[189] G.J. Tatlock, K. Dawson, T. Boegelein, K. Moustoukas, A.R. Jones, High resolution microstructural studies of the evolution of nano-scale, yttrium-rich oxides in ODS steels subjected to ball milling, selective laser melting or friction stir welding, Mater. Today Proc. 3 (2016) 3086–3093, https://doi.org/10.1016/j.matpr.2016.09.024.
[190] R.M. Hunt, K.J. Kramer, B. El-dasher, Selective laser sintering of MA956 oxide dispersion strengthened steel, J. Nucl. Mater. 464 (2015) 80–85, https://doi.org/10.1016/j.jnucmat.2015.04.011.
[191] E. Vasquez, P.F. Giroux, F. Lomello, A. Chniouel, H. Maskrot, F. Schuster, P. Castany, Elaboration of oxide dispersion strengthened Fe-14Cr stainless steel by selective laser melting, J. Mater. Process. Technol. 267 (2019) 403–413, https://doi.org/10.1016/j.jmatprotec.2018.12.034.
[192] R. Gao, L. Zeng, H. Ding, T. Zhang, X. Wang, Q. Fang, Characterization of oxide dispersion strengthened ferritic steel fabricated by electron beam selective melting, Mater. Des. 89 (2016) 1171–1180, https://doi.org/10.1016/j.matdes.2015.10.073.
[193] K. Saeidi, L. Kvetková, F. Lofaj, Z. Shen, Austenitic stainless steel strengthened by the in situ formation of oxide nanoinclusions, RSC Adv. 5 (2015) 20747–20750, https://doi.org/10.1039/C4RA16721J.
[194] F. Yan, W. Xiong, E. Faierson, G.B. Olson, Characterization of nano-scale oxides in austenitic stainless steel processed by powder bed fusion, Scr. Mater. 155 (2018) 104–108, https://doi.org/10.1016/j.scriptamat.2018.06.011.
[195] C. Qiu, A new approach to synthesise high strength nano-oxide dispersion strengthened alloys, J. Alloy. Comp. 790 (2019) 1023–1033, https://doi.org/10.1016/j.jallcom.2019.03.221.
[196] L. Thijs, J. Van Humbeeck, Investigation on the inclusions in maraging steel produced by Selective Laser Melting, in: P.J. Bártolo (Ed.), Innov. Dev. Virtual Phys. Prototyp., 2011, pp. 297–304. http://books.google.com/books?hl=en&lr=&id=Q002_TiMJ6kC&oi=fnd&pg=PA297&dq=Investigation+on+the+Inclusions+in+Maraging+Steel+Produced+by+Selective+Laser+Melting&ots=kfwy9JEg1z&sig=7J18rvghDiO_BCoTp9Omy5Qv1vM. (Accessed 11 April 2014).
[197] Y. Liu, J. Fang, D. Liu, Z. Lu, F. Liu, S. Chen, C.T. Liu, Formation of oxides particles in ferritic steel by using gas-atomized powder, J. Nucl. Mater. 396 (2010) 86–93, https://doi.org/10.1016/j.jnucmat.2009.10.057.
[198] E. Yasa, J. Van Humbeeck, J. Kruth, K. Kempen, M. Rombouts, L. Thijs, Investigation on the inclusions in maraging steel produced by Selective Laser Melting, in: Innov. Dev. Virtual Phys. Prototyp., 2012, pp. 297–304, https://doi.org/10.1201/b11341-48.
[199] X. Zhou, Z. An, Z. Shen, W. Liu, C. Yao, Particles control in selective laser melting in-situ oxide dispersion strengthened method, IOP Conf. Ser. Mater. Sci. Eng. 167 (2016), 012048, https://doi.org/10.1088/1757-899X/167/1/012048.
[200] H. Springer, C. Baron, A. Szczepaniak, E.A. Jägle, M.B. Wilms, A. Weisheit, D. Raabe, Efficient additive manufacturing production of oxide- and nitride-dispersion-strengthened materials through atmospheric reactions in liquid metal deposition, Mater. Des. 111 (2016) 60–69, https://doi.org/10.1016/j.matdes.2016.08.084.
[201] C. Doñate-Buendía, F. Frömel, M.B. Wilms, R. Streubel, J. Tenkamp, T. Hupfeld, M. Nachev, E. Gökce, A. Weisheit, S. Barcikowski, F. Walther, J.H. Schleifenbaum, B. Gökce, Oxide dispersion-strengthened alloys generated by laser metal deposition of laser-generated nanoparticle-metal powder composites, Mater. Des. 154 (2018) 360–369, https://doi.org/10.1016/j.matdes.2018.05.044.
[202] M. Simonelli, C. Tuck, N.T. Aboulkhair, I. Maskery, I. Ashcroft, R.D. Wildman, R. Hague, A study on the laser spatter and the oxidation reactions during selective laser melting of 316L stainless steel, Al-Si10-Mg, and Ti-6Al-4V, Metall. Mater. Trans. A (2015), https://doi.org/10.1007/s11661-015-2882-8.
[203] B. AlMangour, D. Grzesiak, J.-M. Yang, Rapid fabrication of bulk-form TiB2/316L stainless steel nanocomposites with novel reinforcement architecture and improved performance by selective laser melting, J. Alloy. Comp. 680 (2016) 480–493, https://doi.org/10.1016/J.JALLCOM.2016.04.156.
[204] B. AlMangour, Y.-K. Kim, D. Grzesiak, K.-A. Lee, Novel TiB2-reinforced 316L stainless steel nanocomposites with excellent room- and high-temperature yield strength developed by additive manufacturing, Compos. B Eng. 156 (2019) 51–63, https://doi.org/10.1016/J.COMPOSITESB.2018.07.050.
[205] B. AlMangour, D. Grzesiak, J.-M. Yang, In-situ formation of novel TiC-particle-reinforced 316L stainless steel bulk-form composites by selective laser melting, J. Alloy. Comp. 706 (2017) 409–418, https://doi.org/10.1016/J.JALLCOM.2017.01.149.
[206] B. AlMangour, D. Grzesiak, Jenn-MingYang, Selective laser melting of TiC reinforced 316L stainless steel matrix nanocomposites: influence of starting TiC particle size and volume content, Mater. Des. 104 (2016) 141–151, https://doi.org/10.1016/J.MATDES.2016.05.018.
[207] C. Qiu, N.J.E. Adkins, M.M. Attallah, Selective laser melting of Invar 36: microstructure and properties, Acta Mater. 103 (2016) 382–395, https://doi.org/10.1016/j.actamat.2015.10.020.
[208] N.J. Harrison, I. Todd, K. Mumtaz, Thermal expansion coefficients in Invar processed by selective laser melting, J. Mater. Sci. 52 (2017) 10517–10525, https://doi.org/10.1007/s10853-017-1169-4.
[209] M. Yakout, M.A. Elbestawi, S.C. Veldhuis, A study of thermal expansion coefficients and microstructure during selective laser melting of Invar 36 and stainless steel 316L, Addit. Manuf. 24 (2018) 405–418, https://doi.org/10.1016/j.addma.2018.09.035.
[210] X. Zhan, J. Zhou, C. Qi, D. Gu, The influence of heat input on the microstructure and solute segregation mechanism of invar alloy laser melting deposition process, Mater. Res. Express 5 (2018) 116530, https://doi.org/10.1088/2053-1591/aaded2.
[211] M. Garibaldi, I. Ashcroft, M. Simonelli, R. Hague, Metallurgy of high-silicon steel parts produced using Selective Laser Melting, Acta Mater. 110 (2016) 207–216, https://doi.org/10.1016/j.actamat.2016.03.037.
[212] M. Garibaldi, I. Ashcroft, J.N. Lemke, M. Simonelli, R. Hague, Effect of annealing on the microstructure and magnetic properties of soft magnetic Fe-Si produced via laser additive manufacturing, Scr. Mater. 142 (2018) 121–125, https://doi.org/10.1016/j.scriptamat.2017.08.042.
[213] M. Garibaldi, I. Ashcroft, N. Hillier, S.A.C. Harmon, R. Hague, Relationship between laser energy input, microstructures and magnetic properties of selective laser melted Fe-6.9%wt Si soft magnets, Mater. Char. 143 (2018) 144–151, https://doi.org/10.1016/j.matchar.2018.01.016.
[214] C.V. Mikler, V. Chaudhary, T. Borkar, V. Soni, D. Jaeger, X. Chen, R. Contieri, R. V. Ramanujan, R. Banerjee, Laser additive manufacturing of magnetic materials, JOM (J. Occup. Med.) 69 (2017) 532–543, https://doi.org/10.1007/s11837-017-2257-2.
[215] P. Bajaj, J. Wright, I. Todd, E.A. Jägle, Predictive process parameter selection for Selective Laser Melting Manufacturing: Applications to high thermal conductivity alloys, Additive Manufacturing 27 (2019) 246–258, https://doi.org/10.1016/j.addma.2018.12.003.